Department of Precision and Microsystems Engineering

Electrochemical sensing and electrochemical advanced oxidation treatment of nevirapine using micro- and nanocrystalline boron doped diamond electrodes

R.H.J.M. Koldenhof

Report no : MNE 2020.027
Coach : M.Sc. Zhichao Liu
Professor : Dr. J.G. Buijnsters
Specialisation : Micro and Nano Engineering
Type of report : Master Thesis
Date : 03-09-2020

Abstract

Boron-doped diamond (BDD) is an electrode material applied in high end advanced oxidation processes and electrochemical sensing. BDD has a low background current, is robust and has a high affinity for the production of oxidizing radicals. BDD shows better degradation rates compared to competing electrode materials, and can also be used to detect trace amounts of compounds. The surface properties of BDD electrodes, such as the crystal sizes present on the electrode surface and the presence of non diamond content, influence their degradation and sensing performance. Electrochemical advanced oxidation processes using BDD electrodes are one of the methods investigated in literature to remove recalcitrant micro-pollutants from wastewater. Wastewater treatment at present faces a challenge to eliminate micro-pollutants of increasing complexity and toxicity. One of the compounds that could potentially benefit from the application of BDD electrodes in its removal from wastewater and detection in human blood and analogues is nevirapine. Nevirapine (NVP) is an antiretroviral on the World Health Organization's list of essential medicines, used extensively in HIV treatment. NVP has been detected in wastewater in the continents where it is deployed as treatment, and has shown resistance to ordinary wastewater treatment. The removal of NVP from wastewater and the detection of NVP in human blood are current challenges considered in academic research. NVP has not been used in detection or degradation studies using BDD electrodes before.

In this study, two types of electrodes, a micro-crystalline and a nano-crystalline BDD electrodes, were used to attempt to electrochemically degrade and detect NVP. Degradation attempts in 0.39 M NaCl revealed a bathochromic shift in the characteristic UV-Vis spectrum of NVP, which was more pronounced for the micro-crystalline electrode. Detection experimentation in phosphate buffered saline (1X) revealed inhibiting behaviour of NVP on BDD electrodes, which limits the degradation and sensing processes.
Using a detection procedure involving cathodic activation at -2V for 10 s, the inhibition induced by NVP was partially reversed, recovering characteristic peak formation around 2 to 10 μM NVP for the micro- and nano-crystalline electrode respectively, in PBS (1X). The micro-crystalline BDD electrode provided better results in both the attempted degradation of NVP and the sensing of NVP, which is attributable to its high ratio of diamond content compared to non-diamond impurities. The application of electrochemical activation in combination with micro-crystalline BDD electrodes for NVP sensing is a promising lead into new research to detect low concentrations of NVP using in-situ electrode cleaning. The results obtained indicate further research into the interaction between NVP and the surface of BDD electrodes as well as electrochemical activation could provide a stable detection method to asses NVP at levels competitive to those reported in literature. The research into degradation of NVP using BDD electrodes indicates the practical challenges the interaction between NVP and BDD surfaces poses, for the removal of NVP from wastewater using electrochemical advanced oxidation processes.

Contents

Abbreviations

- AFM: Atomic force microscopy
- AOP: Advanced oxidation process(es)
- BDD: Boron doped diamond
- CE: Counter electrode
- CPE: Carbon paste electrode *or* constant phase element.
- CV: Cyclic voltammetry
- CVD: Chemical vapour deposition
- DPV: Differential pulse voltammetry
- EAOP: Electrochemical advanced oxidation process(es)
- EIS: Electrochemical impedance spectroscopy
- GCE: Glassy carbon electrode
- H.I.V.: Human immunodeficiency virus
- HFCVD: Hot filament chemical vapour deposition
- LOD: Limit of detection
- LSV: Linear sweep voltammetry
- MC: Micro-crystalline
- MCD: Micro-crystalline diamond
- NC: Nano-crystalline
- NCD: Nano-crystalline diamond
- NVP: Nevirapine
- PBS: Phosphate buffered saline
- RE: Reference electrode
- SEM: scanning electron microscopy
- UNC: Ultra-nano-crystalline
- UNCD: Ultra-nano-crystalline diamond
- UV-Vis: Ultraviolet-visible
- WE: Working electrode
- WWTP: Wastewater treatment plant

Chapter 1

Introduction

Wastewater pollution is a recurring and increasing problem in modern society. As packaging, pharmaceutical and personal care products advance, more complex and resistant compounds are developed. Many of these compounds end up in wastewater, also through human excretion. The presence of these compounds in aquatic environments has damaging effects to natural flora and fauna. Some of these compounds also present a direct danger towards humans when improperly removed from wastewater. Wastewater treatment plants are increasingly incapable of eliminating compounds dissolved in wastewater. These compounds are usually diluted to low concentrations and are difficult to remove using ordinary treatment procedures. Often, the compounds are toxic to the biological cultures used to treat wastewater. Additional procedures are often considered as a means to eliminate the presence of these advanced compounds by supplementing ordinary procedures. Electrochemical advanced oxidation is one of the procedures currently investigated. In electrochemical advanced oxidation, electrodes are used to produce oxidizing radicals to mineralize pollutants into compounds that can be removed. An interesting electrode material to use for this procedure is boron-doped diamond (BDD). BDD electrodes have been used in electrochemical research to degrade and detect a multitude of micropollutants. The unique surface properties of BDD demonstrate it as an ideal electrode material for multiple applications. In electrochemical degradation applications, BDD has the potential to outlast and outperform most other electrode materials. The robustness and high oxygen evolution overpotential grant BDD a higher performance and potentially extended lifespan. In detection applications, the low background current and wide potential window grant BDD a sensitivity that performs far better compared to conventional electrode materials.

Nevirapine (NVP) is a micro-pollutant extensively used as a medicine in HIV treatment. NVP shows resistance to regular wastewater treatment, and is a current topic in electrochemical detection research. Detection of NVP in human blood by electrochemical detection in a fast and sensitive manner shows considerable promise for routine applications. Electrochemical degradation or sensing of NVP using BDD electrodes has not been reported as of present.

The application of different types of BDD electrodes to the electrochemical degradation and sensing of NVP present several advantages.

Electrochemical advanced oxidation using BDD electrodes could show a reliable and effective way to remove NVP from wastewater, while detecting NVP electrochemically using BDD electrodes could potentially show increased sensitivity compared to the electrodes currently used in research.

This thesis aims to characterize two types of as-grown BDD electrodes, and using them, attempts are made to electrochemically degrade and sense NVP. The performance of the different types of boron-doped diamond for both applications was compared.

The characterisation of the electrodes will be done by scanning electron microscopy, Raman spectroscopy, atomic force microscopy, contact angle measurements, cyclic voltrammery and electrochemical impedance spectroscopy. The performance of the electrodes in degradation and detection respectively was determined using UV-Vis spectrophotometry and differential pulse voltrammetry.

The literature study describing the required background information for electrochemical advanced oxidation, BDD electrodes, NVP and the characterisation methods is in Chapter 2. The research foci can be found in Chapter 3. Chapter 4 details the experimental setup and procedures. Chapter 5 discusses the results and discussion from these procedures.

Chapter 2

Literature review

Relevant literature and preporatory knowledge will be discussed in this chapter.

First, treatment of wastewater through advanced oxidation processes is introduced in Section 2.1.

Second, diamond's unique properties and potential as a doped electrode will be discussed in Section 2.2.

Third, the micropollutant used in this thesis, nevirapine, is introduced in Section 2.3.

The methods to characterize diamond electrodes are discussed in Section 2.4, and the methods to detect nevirapine and its degradation in Section 2.5.

2.1 Micropollutants and advanced oxidation processes

2.1.1 Wastewater pollution by pharmaceuticals

Wastewater from industrial and civilian applications contains many pollutants. From medicines excreted by people to herbicides and plastics, waste water treatment plants (WWTP) have to cope with a variety of substances. WWTPs commonly run a variety of treatments to remove pollutants from the water. Ordinary wastewater treatment procedures include e.g. filtration and microbiology treatment. With the increasing complexity and use of substances in modern life, a growing number of pollutants are not removed by ordinary procedures. Of note are a class of pollutants called micropollutants. Micropollutants are commonly defined as anthropogenic chemicals that appear at low but unnatural concentrations due to human activity [1]. A lot of micropollutants are resistant to regular treatment techniques. A growing body of research deals with removing these micropollutants in a WWTP. Pharmaceutical micropollutants have proven especially hard to remove. Many pharmaceutical micropollutants dissolve in water and are resistant to microbiological removal. Antibiotics, painkillers and antiviral compounds are commonly used compounds that appear in the wastewater entering a WWTP (influent). A high percentage of these substances are also detected in the treated water expelled by the WWTP (effluent).
Pharmaceutical micropollutants are a relevant problem for WWTPs due to the nature of their consumption. Most compounds used in a medicinal setting will be processed and excreted by the human body in multiple ways. This results in the original compound and its processed metabolites appearing at influent in a WWTP. Most pharmaceutical micropollutants are detrimental when present in the natural water environment or processed water. Many pharmaceutical micropollutants are also toxic to microcultures and small lifeforms, creating ecological damage. Specific pharmaceuticals also lead to other unwanted effects when present in the ecosystem. For example, antibiotics leaking into the environment can lead to bacterial cultures or humans developing resistance to the antibiotics. A large amount of these micropollutants are also persistent in aquatic environment. They may also persist in the bodies of fauna, causing bioaccumulation. Pharmaceutical micropollutants make up a significant majority of the micropollutants found in wastewater near civilian populations [2]. For specific compounds this varies with geographical importance or seasonal use. Pharmaceutical micropollutants include a wide variety of compounds exhibiting totally different characteristics. Solubility, toxicity and resistance to ordinary treatment processes vary widely. Due to these complications, alternative water purification methods are often considered to remove pharmaceutical micropollutants.

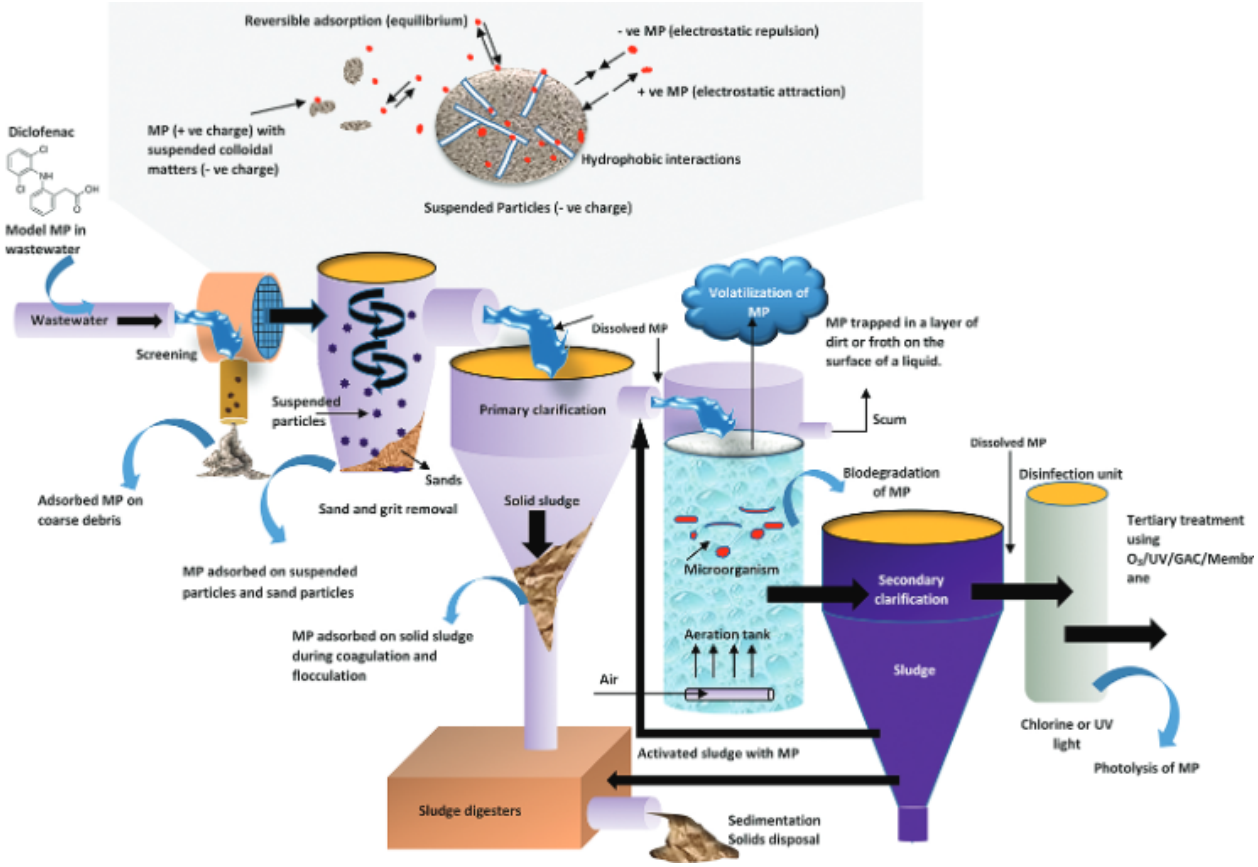

Figure 2.1: A schematic example of a WWTP and the different ways in which it can attempt to remove a pharmaceutical micropollutant (diclofenac). Reproduced from Das et al. [2].

Ordinarily, water purification in a WWTP counts many steps, as illustrated in Figure 2.1. Initially, micropollutants can end up being adsorbed and removed in the processes used to remove sedimentation and suspended particles from the water. Many pharmaceutical micropollutants do not seem to be reliably removed by these processes. After these initial procedures, the water undergoes up to three processes, primary, secondary and tertiary treatment. In the primary treatment process, suspended and colloidal particulates are removed using coagulants. Secondary treatment is the removal of dissolved organics using aerobic micro-organisms in suspension. Tertiary treatment processes are additionally needed by WWTPs that deal with influents that aren't removed using the primary and secondary procedures. Today, tertiary treatment processes are increasingly more relevant to deal with the complex array of modern micropollutants. Examples of tertiary treatment process include ozonisation, advanced carbon adsorption or advanced oxidation.
Pharmaceuticals commonly evade primary and secondary treatment and show up in the effluent of WWTPs. Due to this phenomenon, tertiary treatment is increasingly investigated to accommodate the expanding scope of micro-pollutants WWTPs have to remove.

2.1.2 Electrochemical advanced oxidation processes

Advanced oxidation processes (AOPs) are procedures often considered as tertiary treatment for wastewater laced with pharmaceutical micropollutants. AOPs are a class of oxidation techniques (an overview of the different AOPs is illustrated in Figure 2.2). Oxidation techniques in general rely on the oxidation of the micropollutant to break it down into smaller compounds. By continuously breaking down the micropollutant, eventually more "benign" or removable substances such as carbon dioxide or water and other inorganics can be formed [4].
AOPs specifically are characterised by their production of hydroxyl radicals ($OH^{\bullet}$) (or other radicals or

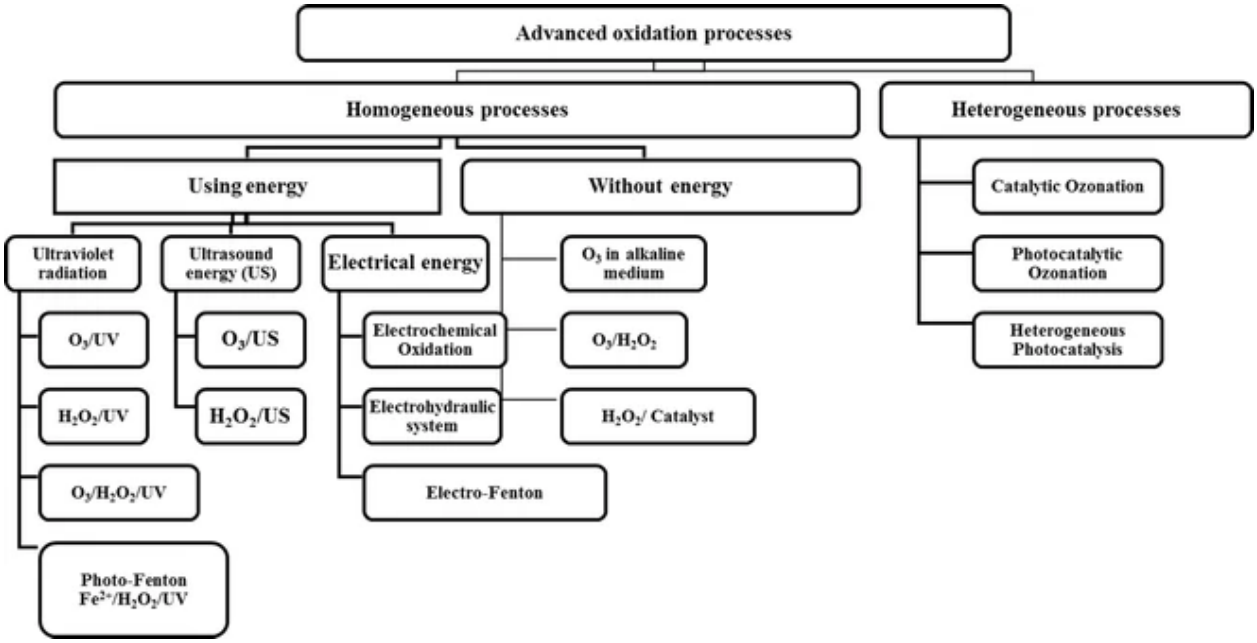

Figure 2.2: An overview of different advanced oxidation processes used to remove pollutants from water. Reproduced from Tijani et al. [3].

oxidizers such as sulfate radicals ($SO_4^{\bullet -}$) or ozone (O_3)). Hydroxyl and sulfate radicals are highly reactive, and attack organic molecules indiscriminately. The production of radicals such as (primarily) the hydroxyl radical is an effective tool when dealing with compounds not removed through most primary or secondary treatment procedures. Hydroxyl radicals and oxidizing species can be produced in many ways by AOPs, using specific chemical reactions, light or electrical processes.
Of the different radicals and oxidants that can be produced during AOPs hydroxyl radicals are especially non-selective, and react rapidly. Hydroxyl radicals can react chemically with compounds in multiple ways to break down larger organic compounds into increasingly smaller varieties. Due to their reactivity, hydroxyl radicals have a short lifespan, and need to be generated in-situ to be used effectively. One of the methods is using an electrode. This variation of AOP (electrochemical advanced oxidation process (EAOP)) is a variation of ordinary electrochemical mineralization using electrodes. Ordinary mineralization relies on direct oxidation on the electrode surface, which requires the substance to make contact with the electrode, making the process slower and the electrode susceptible to fouling [5]. The use of hydroxyl radicals allows for indirect oxidation. In this process, the radical, either adsorbed on the electrode surface in one of several manners or present in the solution very close to the electrode, initiates the oxidation instead of the electrode itself. This lowers the chance of fouling the electrode, and allows the electrode surface to produce radicals when not oxidizing pollutant.
The electrochemical production of hydroxyl radicals involving the initial discharge of water at the electrode surface can be done in two major ways depending on the interaction between the electrode material and hydroxyl radical. These are the electrical activation of water by dissociative adsorption or electrolytic discharge (this will be discussed in Section 2.2.2).

2.2 Boron-doped diamond as electrode material

2.2.1 Diamond

Diamond as a material posseses unique material properties which are highly coveted in multiple applications. From simple jewellery to high performance cutting tools, the unique hardness of diamond allows it to be used in applications where other materials would fail. Diamond derives its unique properties from its unique

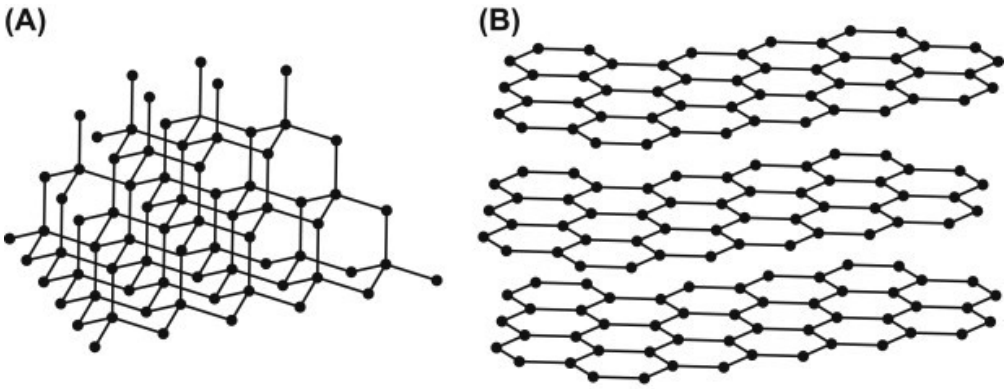

Figure 2.3: The crystal structures of diamond (A) and graphite (B). Adapted from More et al. [6].

crystal structure, illustrated in Figure 2.3. Diamond is composed of the element carbon, arranged in a tetrahedral configuration where each carbon atom is connected to 4 other carbon atoms by covalent bonds. This formation places the carbon atoms at equidistant lengths from each other and, once imposed, provides a very stable and rigid configuration. The diamond unit cell contains 8 of these atoms in a cubic arrangement. In electrochemical research a common allotrope of carbon, graphite, is also relevant. Graphite's crystal structure contains planes of carbon atoms (graphene layers as observed in Figure 2.3) with each atom bound to three neighbours, each 120 degrees apart. The differences between these two configurations are often referred to with their form of hybridization patterns being sp^3 vs. sp^2. For diamond, a tetrahedral configuration, this would be the sp^3 form, and for the trigonal planar geometry of graphite the sp^2 form. The sp^3 diamond formation is more resistant to duress than the sp^2 graphite formation. The sp^2 crystal layers are held together by weak stacking interactions. These layers are easier to shift and dislocate. Diamond does not normally conduct electrons due to the lack of free spots for electrons in the crystal lattice, whereas graphite has delocalised electrons that are free to move within the planes. Ordinarily, at room conditions, graphite is the more stable form of carbon. However, the high energy demand needed to transform from diamond to graphite keeps diamond from reverting to graphite. This results in diamond being metastable at room conditions. To form diamond, high temperature and pressure conditions are required. In natural diamond formation, these conditions are provided at specific locations deep in the earth's crust, the resulting diamond material being delivered to the upper surface periodically by magma. Synthetic diamond creation therefore faces a challenge in reproducing these extreme conditions. To grow single-crystal gemstones, the direct approach is often taken in a so called "high-pressure high-temperature" method. In this method, graphite is heated and compressed to mimic the conditions used to grow natural diamond in a process with considerable energy expenditure. However, if the application the diamond is intended for only needs a film of diamond, chemical vapour deposition (CVD) methods can be employed. In CVD, heat is used to grow diamond crystals using carbon containing gases. After growing through CVD, thin film diamond can express a wide variety of surface characteristics. Different types of crystallinity can be formed this way [7]. These range from micro-crystalline diamond (MCD), which commonly contains grain sizes larger then 1 μm, to ultra-nano-crystalline diamond (UNCD) which commonly exhibits grain sizes smaller then 10 nm. In between, nano-crystalline diamond (NCD) is also commonly defined with grain sizes ranging between 1 μm and 10 nm. Example images of these surfaces can be found in Figure 2.8 in Section 2.4. The growth process and crystallographic orientation also determine where the boron will end up concentrated. Poly-crystalline surfaces will end up heterogenously doped. Non-diamond carbon (NDC), will also be formed and incorporated into the film, and will end up predominantly along the grain boundaries of the diamond content. As NDC and UNDC contain relatively more grain boundaries, NDC plays a larger role on those surfaces in electrochemistery. NDC content usually contains sp^2 carbon. CVD techniques for MCD have at present developed to an extent that NDC content formation can largely be avoided.

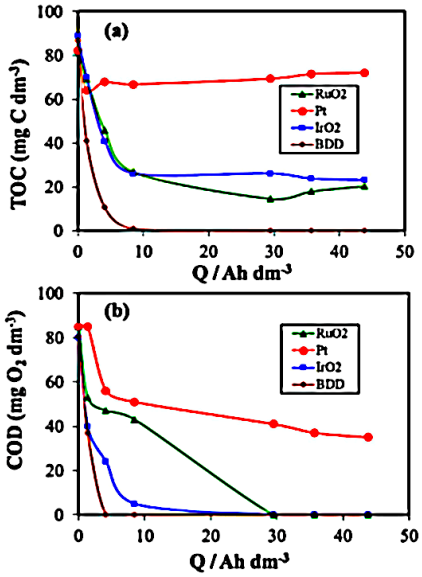

Figure 2.4: Changes in total organic carbon (TOC in graph *a*) and chemical oxygen demand (COD in graph *b*) reported by Dbira et al. [8] during an EAOP treating urine wastewater using different electrodes. The TOC signifies the amount of pollutants mineralized, while the COD value tracks the amount of oxidation occuring.

2.2.2 Boron-doped diamond electrodes

Boron-doped diamond (BDD) is an electrode material with intriguing properties for electrochemical research. BDD has attributes that make it interesting for use in electrochemical detection or AOP. Specifically, the following properties are associated with BDD in comparison to other electrode materials:

1. The ability to endure extreme potentials, allowing the electrode to operate under high potentials without breaking down.
2. A wide solvent window, allowing the electrode to operate under harsher conditions without oxidizing or reducing.
3. A high resistance to corrosive, high pressure and high temperature environments.
4. A high affinity towards the production of OH radicals, characterised by a high over-potential for oxygen evolution.
5. Reduced fouling properties compared to other electrodes.
6. Biocompatibility in sensing applications.
7. Conductivity on the metalic level depending on the doping conditions (e.g. Figure 2.5)

Each of these conditions is influenced by the composition and makeup of the BDD surface. Doping diamond is most commonly done using phosphor or boron. The addition of these elements into the diamond lattice will either create a free electron (N-type doping), or provide a hole for an electron (P type doping). N type dopants (usually larger atoms) are harder to fit into the diamond lattice, whereas the smaller boron atom has an easier fit. This results in CVD processes using a boron containing gas in order to grow BDD thin film. Doping diamond allows the unique chemical properties of diamond to be exploited for the formation of hydroxyl ($OH^{\bullet}$) radicals.
The formation of hydroxyl radicals is affected by the non-active electrode properties of the BDD material. Active electrode materials have a strong interaction between the anode and the generated hydroxyl radicals, which causes the formation of higher state oxides or superoxides [5, 10]. In this case , the radicals

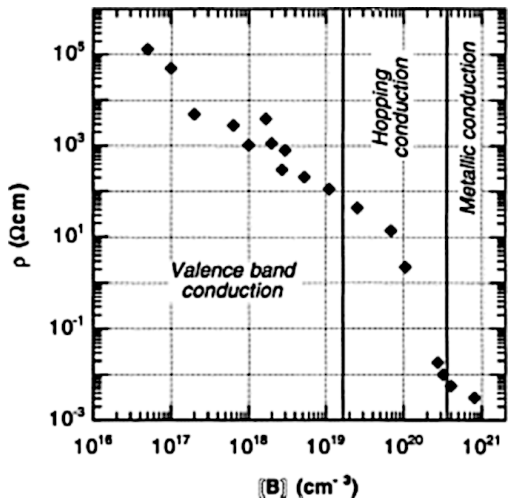

Figure 2.5: Resistivity changes observed by Lagrange et al. [9] in differently doped BDD samples at room temperature. The study observed three types of conduction mechanisms depending on the doped boron concentration in atoms per cubic centimeter.

are chemisorbed and limited to the electrode surface. Non-active electrodes do not show this interaction, and limit their activity to the production of radicals through electrolytic discharge. This is illustrated in Equation (2.1). Here, M is the electrode, and $M(OH^{\bullet})$ indicates hydroxyl radicals on the surface of the electrode. These radicals are intermediates into oxygen evolution as seen in Equation (2.1). Electrogenerated electrolytic hydroxyl radicals can either react with reagents present in water near the electrode as shown in Equation (2.2) (here, $R_{(aq)}$ is the dissolved reactant), or as shown in Equation (2.3).

$$H_2O + M \rightarrow M(OH^{\bullet}) + H^+ + e^- \tag{2.1}$$

$$2R_{(aq)} + M(OH^{\bullet})_n \rightarrow M + \text{Oxidation products} + nH^+ + ne^- \tag{2.2}$$

$$M(2OH^{\bullet}) \rightarrow M + O_2 + 2H^+ + 2e^- \tag{2.3}$$

$$2OH^{\bullet} \rightarrow H_2O_2 \tag{2.4}$$

Equation (2.3) is also referred to as "oxygen evolution". If a non-active electrode has a large oxygen evolution overpotential, the radicals are very weakly bonded (physisorbed). The weaker interaction between the electrode surface and hydroxyl radicals, the slower Equation (2.3) is, and therefore, the more hydroxyl radicals will be present near the electrode to initiate Equation (2.2) instead. Due to its high oxygen evolution overpotential, BDD can produce more hydroxyl radicals comparative to other electrodes. The radical interaction with the BDD surface is remarkably low, comparative to other non-active electrodes, and allows the radicals to be considered quasi-free [5, 11]. The high oxygen evolution overpotential of BDD can even result in the formation of hydrogen peroxide at the electrode surface (illustrated in Equation (2.4)) which is then either oxidized at the electrode or reacts with reagents in the water. Boron doped diamond therefore "attacks" micropollutants in multiple ways compared to normal active electrodes (illustrated in Figure 2.6). All of the aforementioned properties allow BDD to achieve remarkable degradation capacities as demonstrated in Figure 2.4.

The fouling resistance of BDD electrodes is heavily dependant on the type of fouling, and the interaction between the fouling agent and the BDD surface. BDD is heavily resistant against biofilm fouling, but one of the more common fouling methods on electrodes is adsorption based fouling or alternatively, fouling based on the polymerization of oxidized adsorbed pollutants. Although these kinds of fouling occur more often at electrodes that rely on direct oxidation alone, BDD is not immune. The surface of the BDD electrode therefore plays a role in fouling. Certain fouling agents adsorb at comparatively low adsorption rates on sp^3 carbon as compared to other electrode materials [13]. High boron-doping and formation of defect

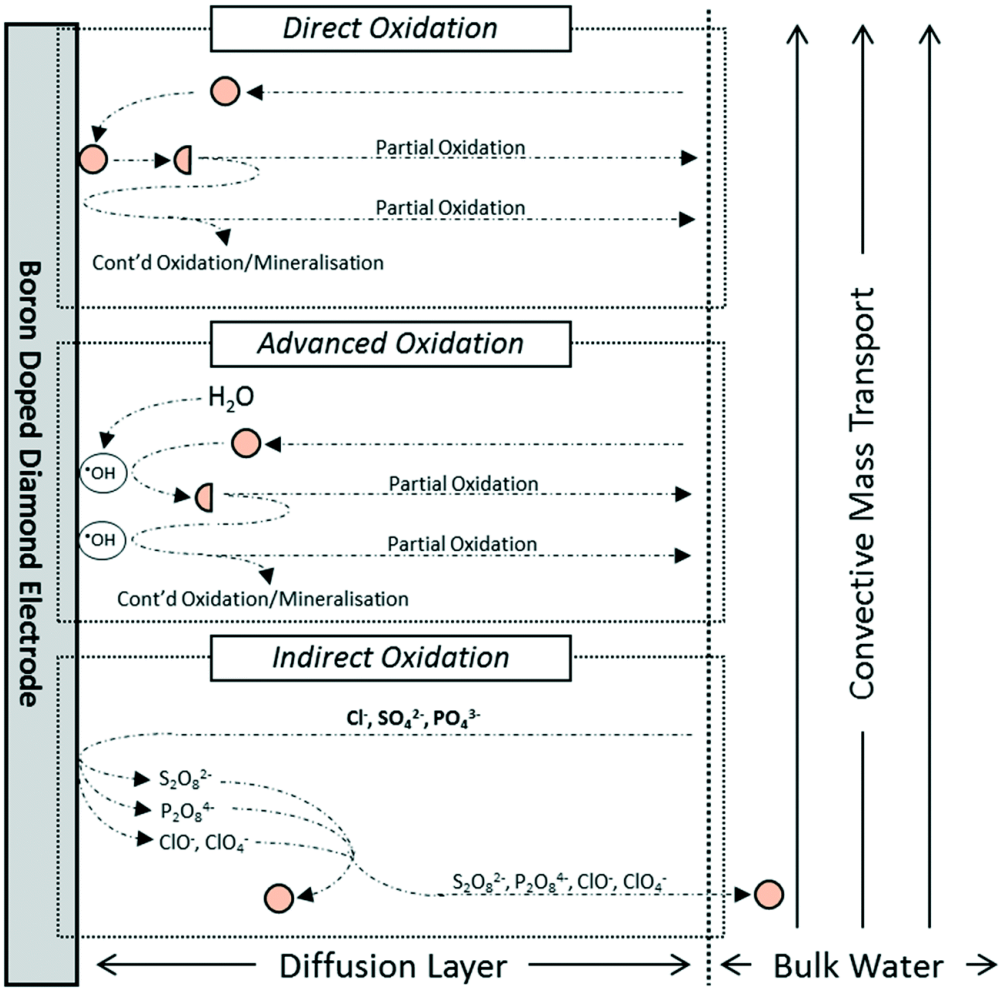

Figure 2.6: The main ways in which BDD electrodes electrochemically degrade micropollutants, reproduced from McBeath et al. [12]. Pollutant is indicated by a salmon dot, intermediate products as a half-dot.

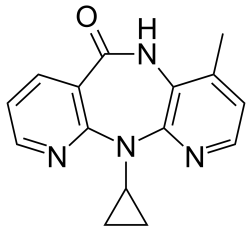

Figure 2.7: The chemical structure of nevirapine ($C_{15}H_{14}N_4O$).

sites have also been observed to diminish the anti-fouling properties of BDD electrodes for e.g. albumin fouling [14]. Surface termination and roughness influence the fouling of BDD electrodes depending on the potential fouling agent. An example of can be found in the study into the adsorption of methyl viologen and anthraquinonedisulfonate at diamond electrodes by Shpilevaya and Foord [15]. Oxygen terminated BDD was found to inhibit the adsorption of the compounds, while hydrogen terminated BDD did not inhibit adsorption.
A minor note is that all of these processes rely on a closed electrochemical circuit, which means that there should be an anode *and* a cathode. At the cathode, electrochemical reduction can take place. This process offers significantly less benefits compared to electrochemical oxidation. Therefore the material properties of the cathode are usually not of as much interest as the anode material properties. The exposed surface and total conductivity of the cathode do however limit the transfer of electrons back into the solution (e.g. Equation (2.5)), so the cathode should always be considered as a limiting factor to the anodic reactions.

$$O_2 + 4H^+ + 4e^- \rightarrow 2H_2O \tag{2.5}$$

From research perspectives, the role of sp^3 and sp^2 carbon in the EAOP on BDD electrodes has significant interest. The sp^3 diamond content is generally held to be preferable for degradation purposes [16]. The sp^3/sp^2 ratio affects the production of hydroxyl radicals [17]. NDC does not share the resistance of sp^3 carbon against chemical reactions, and can be oxidized or affected by processes at the electrode surface. The amount of boron doping also affects how the boron is incorporated in the sp^3 crystal, and can cause sp^2 impurities [18]. These sp^2 impurities affect the background current, potential window and molecular adsorption on the electrode [19]. It is therefore important to characterise this ratio when comparing different BDD electrodes.

2.3 Nevirapine

2.3.1 Nevirapine as a pharmaceutical pollutant

Nevirapine (NVP), illustrated in Figure 2.7, is a non-nucleoside reverse transcriptase inhibitor (NNRTI). Developed by Boehringer Ingelheim Pharmaceuticals and originally sold under the trade name Viramune®, NVP is used in the treatment of HIV. As an NNRTI substance NVP inhibits the activity of the reverse transcriptase enzyme used by retroviruses to transcribe the viral RNA into the DNA of infected cells. NVP treatment effectively slows the spread and growth of HIV in HIV patients. In this capacity, NVP sees use in HIV treatments over multiple continents and has been approved by the WHO as an essential medicine up to as of date. It is recommended to use NVP as part of a drug package consisting of similar antivirals such as stavudine and lumivadine in "highly active antiretroviral therapy" (HAART)[20]. HAART minimizes the occurrence of adverse effects such as viral resistance when using NVP. NVP is usually provided in a drug combination package in the form of an ingestible tablet or oral suspension. HIV treatment using NVP are protracted and remnants of NVP can be found inside the body for prolonged times [21]. NVP is transformed into a variety of metabolites in the body, and a small amount of the drug leaves the body unchanged [22], partly through excretions. These facts and NVP's resistance to biodegradation lead to NVP detection in surface water in countries using it extensively [23–25].
NVP leaking in wastewater presents several undesirable effects [26]. NVP resists biodegradation and is toxic, inhibiting and endangering the activated slug bacteria used in wastewater treatment plants (WWTPs).

Concerns about the effects of antiviral compounds leaking into wastewater are an ongoing body of research that require attention [27]. Bioaccumulation of NVP in selected species (e.g. rats or potentially fish [28]) can lead to toxicity due to the long half-life of NVP. As NVP can extensively persist in the environment, this presents an immediate concern.
NVP has been detected in treated and untreated wastewater from WWTPs [24, 25, 29]. It seems to pass through the processes unscathed due to the aforementioned toxicity and refractory problems thus inhibiting biological treatment. Procedures such as chlorination or UV degradation appear ineffective [29]. Alternative procedures such as AOP are therefore a worthwhile consideration to apply in WWTP as a tertiary treatment to eliminate NVP metabolites and similar antiviral substances.

2.3.2 Electrochemical research on nevirapine

Studies on the degradation of NVP using AOP can not be found in the scientific literature, but electrochemical oxidation procedures have been applied to detect NVP in human serum [20, 30], urine [20] and various electrolyte solutions (NaOH and phosphate or Britton-Robinson buffers as seen in Table 2.1).

Table 2.1: Prevalent studies on electrochemical detection of NVP (abbreviations in Appendix), reproduced from Ahmadi et al. [32] and expanded.

Electrode	**Detection Technique**	**Electrolyte**	**Linear range (μM)**	**LOD μM**	**pH**	**Reference**
Hg-GCE	ASV	0.01 M NaOH	0.04-0.5	0.003	11.3	[31]
MHHC-AgNPs /MWC-NTs/GCE	Amperometry	0.01 M NaOH	0.05-21	0.014	12	[32]
$CP - Bi_2O_3$	DPV	0.2 M phosphate buffer	0.05-50	0.11	8	[20]
TiO_2 /GN-R/GCE	DPV	0.1 M phosphate buffered saline	0.02-0.14	0.043	11	[33]
Ura/CPE	DPV	0.1M NaOH	0.1-70	0.05	13	[30]
AuNPs/p(MB) /MWC-NTs/GCE	DPASV	-	0.1-50	0.056	11	[34]
CuO-CNPs-GCE	LSV	phosphate solution	0.1-100	0.066	7	[35]
GCE	DPV	phosphate buffer	5-350	1.026	10	[36]
AuE	DPV	Britton-Robinson buffer	1.1-3.8	-	2	[37]

Probable reaction mechanisms for electro-oxidation of NVP during detection have been suggested before by Teradal and Seetharamappa [20]. Research on NVP detection focuses primarily on Differential Pulse Voltammetry (DPV) and is frequently performed in phosphate buffer solutions or NaOH solutions of different pH values. NVP has been succesfully detected at different electrode materials, but as of current not on a BDD electrode. Previous studies reveal linear detection ranges roughly between 0.1 to 100 - 400 μM demonstrating detection limits generally as low as 0.05 μM for different electrodes. The electrochemical behaviour exhibited by NVP appears irreversible and pH-influenced, with detection behaviour frequently reported to increase around base pH values (10 - 13). Detection around neutral pH (7-8) is also reported. Previous anodes used for NVP detection include modified carbon paste electrodes and glassy carbon electrodes with different surface modifications to increase detection capability. Use of BDD, resistant to fouling and demonstrating a low background current, could offer a powerful, albeit unselective anode for electrochemical detection. Detection around the levels of NVP wastewater pollution reported in Nairobi river basin [24] have only been reported using a glassy carbon at pH 11.3 using a mercury anodic stripping differential pulse voltammetry. More common detection limits for electrochemical detection are reported around 0.05 μM NVP. NVP detection

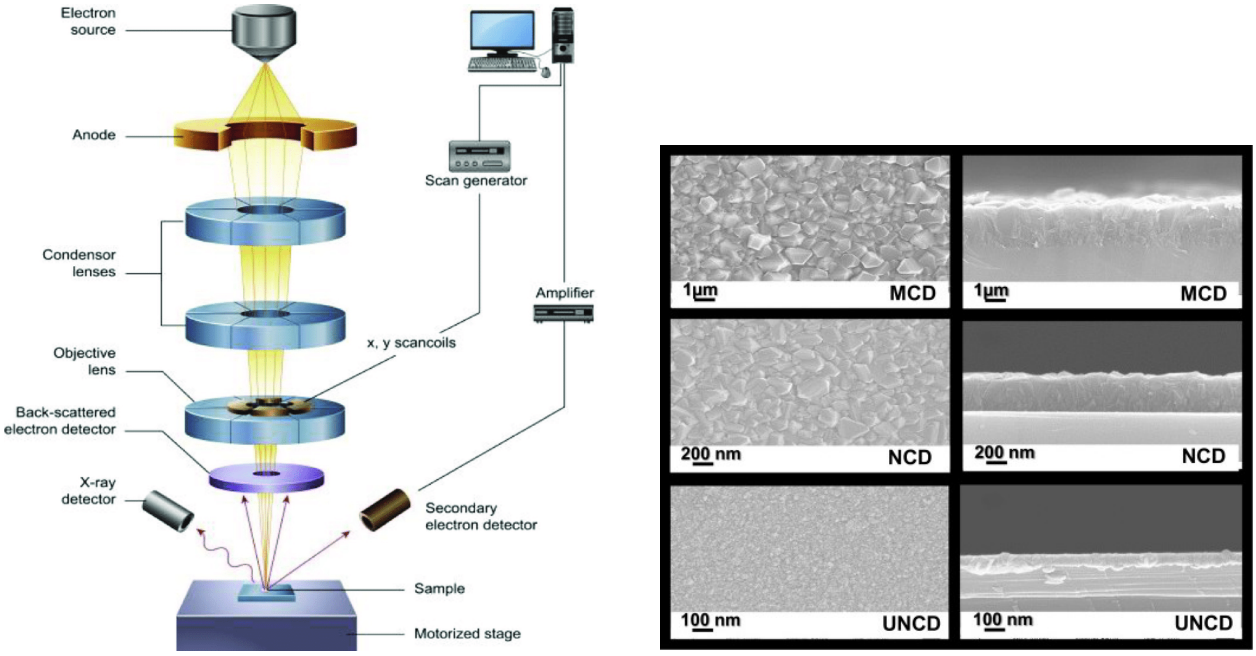

(a) (b)

Figure 2.8: (a): A schematic view of a SEM with multiple detection methods, reproduced from S. Ali [38]. (b) Different top (left) and side-plane (right) views of thin-film diamond crystal size variations in SEM images, adapted from Montes-Gutiérrez et al. [39].

directly in wastewater is currently still commonly done using methods with more sensitive detection limits (e.g. mass spectroscopy) [36]. The application of electrochemical NVP detection could provide advantages for the detection of NVP in biological samples from fauna or humans such as blood plasma or actual blood samples. BDD with a low background current provides high sensitivity for biosensor application, and could, potentially be applied to the sensitivity level required for wastewater detection if optimized.

2.4 Electrode characterisation methods

2.4.1 Surface topography characterisation methods

Scanning Electron Microscopy

Scanning electron microscopy (SEM) works by probing the surface of a sample with a focused beam of electrons. When the electrons strike a sample they interact with the atoms in the sample due to their kinetic energy. The energy dissipated in this way results in the production of various signals such as backscattered electrons or secondary electrons. All of these signals can be measured to obtain information about the surface topography and composition of the sample. Backscattered and secondary electron signals are commonly used for sample imaging. A schematic image of a SEM setup can be seen in Figure 2.8a. MCD, NCD and UNCD have different visible crystalline characteristics in SEM imaging, as shown in Figure 2.8b.

Atomic Force Microscopy

In atomic force microscopy (AFM), a microscopic cantilever with a sharp tip interacts with the surface of a sample. A laser beam is reflected off the back of the cantilever to track the change in cantilever position (as shown in Figure 2.9). Depending on the proximity of the cantilever to the sample surface, different forces will act on the cantilever, causing a deflection. The three major AFM operating distinctions are contact mode, intermittant contact mode and non-contact mode. Contact mode allows operations such as dragging

the tip across the surface. In intermittent contact mode, a cantilever touches the sample at intervals in a tapping behaviour. In non-contact mode the cantilever tip interacts with forces that are introduced due to getting within close proximity of the sample such as the van der Waals forces.

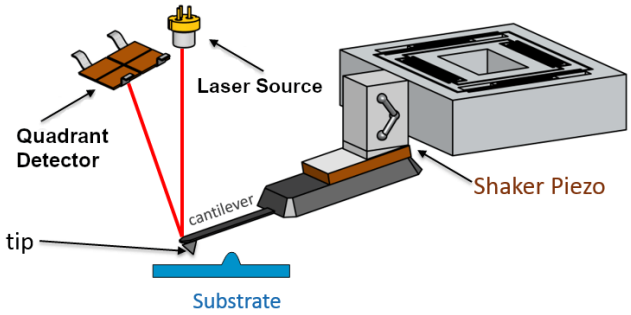

Figure 2.9: A schematic of the workings of an AFM using a red laser. Adjusted from Nanosurf AG [40].

Raman Spectroscopy

Raman spectroscopy is highly recommended as a method to classify the quality of a BDD electrode [7]. Raman spectroscopy operates by shining a laserlight on the sample surface and analyzing the laserlight that is returned after interacting with the surface (as shown in Figure 2.10). When the laser light hits the surface, some of the laser light photons will undergo inelastic scattering (Raman scattering). This results in these photons interacting with the molecular vibrations in the surface layer and the photons show a shift in energy levels. The photons are then absorbed, transmitted or backscattered by the sample. By filtering the backscattered photons from the original wavelength of the laser, the photons that interacted with the sample surface can be selectively detected. The resulting characteristic spectral profile can be used to classify materials. Thin-film BDD has characteristic Raman behaviour that allows its carbon makeup and boron concentration to be assessed. Three peaks, sometimes called bands, if not clearly discernible as peaks, in particular are specific to BDD analysis: the B, G and D peaks. These are the boron related peak, the graphite related peak and the disordered carbon related peak. The G and D peaks are influenced by NDC, whereas the boron peak is influenced by the local boron content due to Raman scattering involving B-C vibrational modes [41, 42]. "Pure" diamond with only sp^3 carbon shows as a single peak at a wavenumber of 1332 cm^{-1}. The relative shapes of these peaks are distinctively different between MCD, NCD and UNCD.

Contact angle measurement

Using a camera and a defined drop of water, it is possible to determine the contact angle of a water droplet on the BDD surface. The contact angle on a BDD surface is related to its hydrophobic or hydrophilic behaviour. This in turn is directly related to the surface termination of the BDD surface. Hydrogen terminated BDD (BDD with hydrogen as the functional group exposed on the surface, which is the termination it has upon leaving the growth chamber), is hydrophobic and has high contact angles (e.g. 90 degrees). Over prolonged periods in time or in electrochemical experiments, the surface oxidizes and turns oxygen terminated (BDD with oxygen as the functional group exposed on the surface). Oxygen terminated BDD is more hydrophilic compared to hydrogen terminated BDD. Oxidized surfaces will have contact angle ranges from 0.6° to 65° degrees depending on the method and roughness of the surface [7]. It is therefore possible to infer the termination using the contact angle test for hydrophobic behaviour.

2.4.2 Electrochemical characterisation methods

CV Characterisation

Cyclic voltammetry (CV) is an experiment setup in which the current is measured while the applied potential in an electrochemical cell is cycled in a set pattern. To properly perform this procedure an electrochemical cell should at least contain a working electrode (WE), reference electrode (RE) and counter electrode (CE).

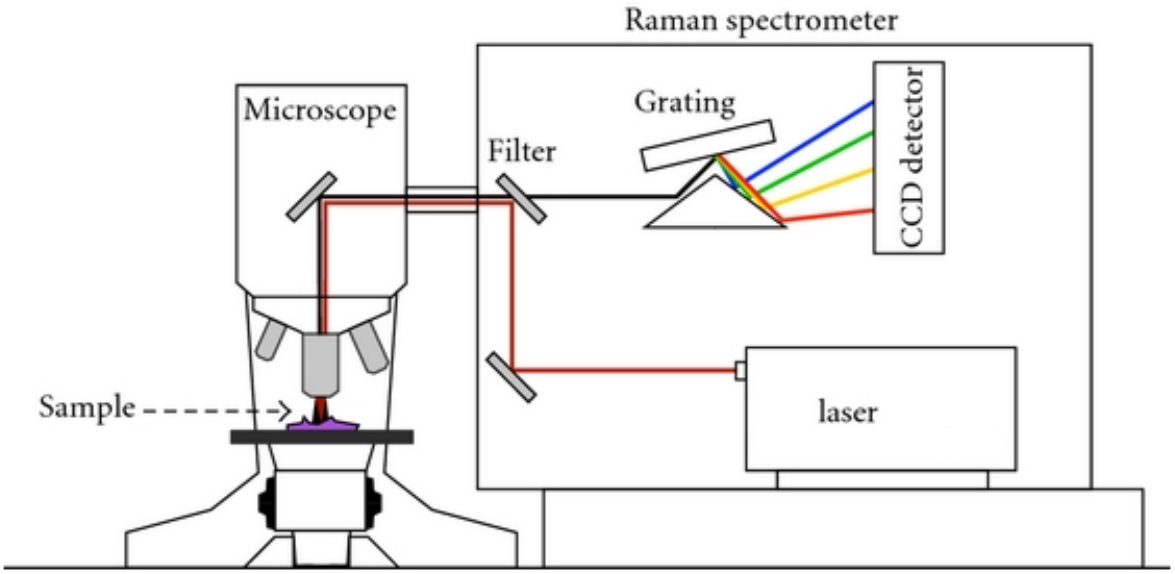

Figure 2.10: Depiction of a micro-Raman spectroscopy setup. Adapted from Xanthopoulos et al. [43].

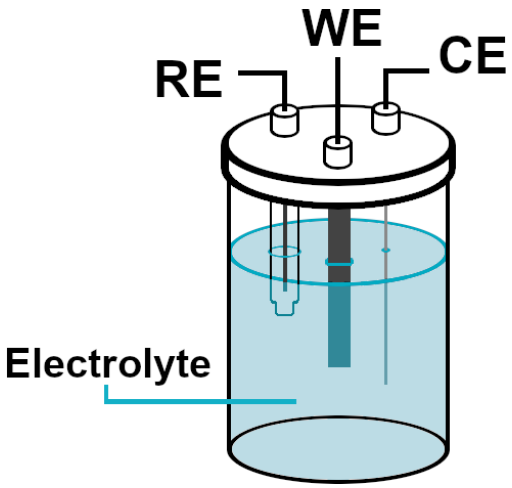

Figure 2.11: A depiction of a three-electrode cell.

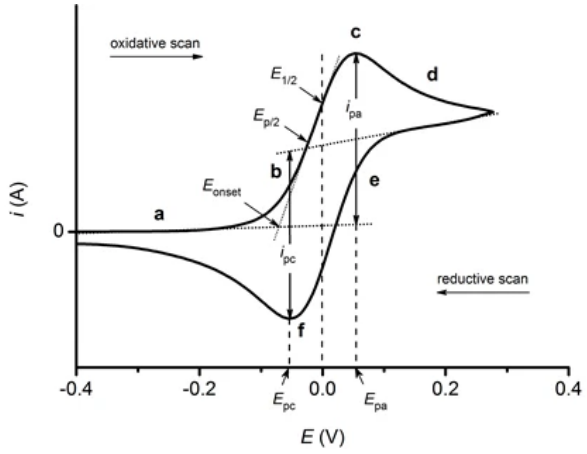

Figure 2.12: An example of a "Duck-shaped " cyclic voltammogram and the baselines extrapolated to record different peak values. Reproduced from Ossila Ltd [44].

Using a potentiostat, a three-electrode setup can be formed (illustrated in fig. 2.11). In this common setup, two modes are discerned, potentiostatic and galvanostatic mode.
In potentiostatic mode, the potential difference between the WE and CE is controlled so that the difference in potential between the WE and RE, also called the "applied potential", is defined. Meanwhile the current at the CE is manipulated. The current flowing between the WE and CE is measured during this manipulation. In galvanostatic mode the current between the WE and CE is controlled while both this current and the applied potential are measured.

When a species in the electrochemical cell reacts due to the applied potential, it increases the current demand which results in a peak in the measured current. A species that has a redox couple will result in two observable peaks in the CV. These peaks are called the anodic and cathodic peak. The anodic peak is associated with oxidation of the species, and appears while the potential is swept upwards. The cathodic peak is associated with reduction and appears when the potential is swept downwards. By extrapolating baselines from the background baselines the peak current can be measured, as illustrated in Figure 2.12.
The speed at which the potential changes, called the scan rate, can influence the peak height and position. If a redox reaction is reversible on the WE surface, increasing the scan rate will increase the peak-to-peak height at higher scan rates. If a redox reaction is quasi reversible or irreversible at the surface of the WE, the peaks move apart as well.

One of the dominant reported values to quantify electrode material performance is the electron transfer rate constant k_0. It provides an indication of the speed of electron transfer between an electroactive species and an electrode surface [45]. It also indicates the overall electrochemical performance.
For BDD electrodes, the k_0 is directly or indirectly affected by all of the surface properties of the BDD, e.g. boron doping level and distribution, NDC and sp^3/sp^2 ratio. The electron transfer rate constant is often determined using Nicholson's method [46, 47]. In this method the transfer rate is calculated for a quasi or irreversible process that ascribes to certain conditions. Nicholson's method relies on the peak to peak potential difference (ΔE_p) as a function of the dimensionless kinetic parameter ψ. As long as the transfer coefficient α is within a range of 0.3 to 0.7, which is common for simple electron transfer reactions, ΔE_p will act as if independent of α. α can be calculated as in eq. (2.6) using R as the gas constant (8.314 J/(molK)), T as the temperature in Kelvin, F as the Faraday constant (96485.33 C/mol) and $E_{p/2}$ as the half-peak potential in V. Moreover, if the diffusion coëfficients of oxidized and reduced species D_O and D_R are similar, the k_0 value can be calculated from eq. (2.7). In this equation υ is the scan rate in V/s. The value of Nicholson's kinetic parameter can be derived from the ΔE_p using different methods. Most common is a table of predetermined values.

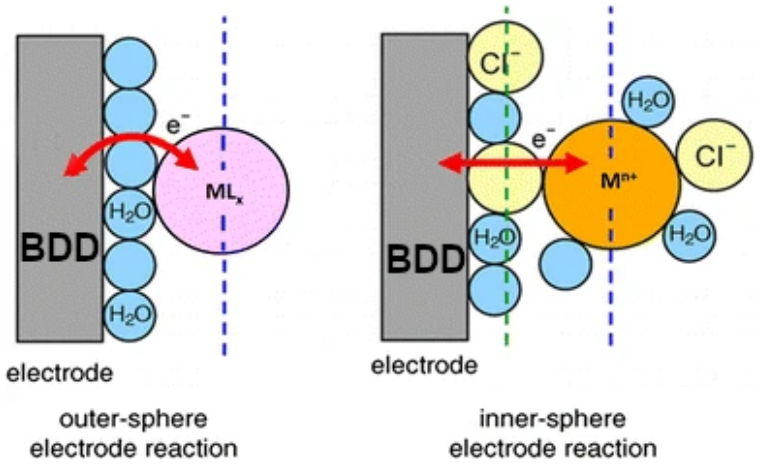

Figure 2.13: A schematic of the difference between inner and outer sphere electron transfers. Adapted from Seeber et al. [48].

$$\alpha = \frac{1.857RT}{F|\Delta E_p - E_{p/2}|} \tag{2.6}$$

$$\psi = \frac{(\frac{D_O}{D_R})^{\frac{\alpha}{2}} k_0}{(\frac{\pi D_O v F}{RT})^{\frac{1}{2}}} \tag{2.7}$$

The electron transfer rate can also be estimated using electrochemical impedance spectroscopy.

Ferrocyanide and ruhex as redox couples

Ferrocyanide ($Fe(CN)_6^{4-}$) and ruhex ($Ru(NH_3)_6^{3-}$) are often used to characterize electrode behavior. These species have specific redox reactions that are known and result in characteristic cathodic and anodic peaks that indicate the oxidative or reductive reactions at the electrode surface. These reactions are $Fe(CN)_6^{4-} \rightleftharpoons Fe(CN)_6^{3-} + e^-$ and $Ru(NH_3)_6^{3-} \rightleftharpoons Ru(NH_3)_6^{2-} + e^-$. Ferrocyanide and ruhex are respectively used as an inner and outer sphere redox couple. When an electronic conductor (e.g. an electrode) is exposed to an ionic conductor with a different phase (e.g. an electrolyte solution), an interface of ions forms on the electrode surface. These ions are called "specifically adsorbed ions". Inner and outer sphere redox couples interact differently with this layer of specifically adsorbed ions as shown in Figure 2.13. This layer, combined with the opposite polarity attracted ions in the solution, is also indicated as the electronic double layer (EDL).

Ferrocyanide undergoes inner-sphere electron transfer. In this process the electron transfer takes place at the same layer as the specifically adsorbed ions, called the Inner Hemholtz plane. Here the reaction takes place without the monolayer of ions, using a ligand adsorbed on the electrode surface. As a result, the electrode transfer for a ferrocyanide redox reaction is highly sensitive to the electrochemical surface characteristics of the electrode.
Ruhex undergoes outer-sphere electron transfer. The electron transfer for ruhex occurs fast and the electron hops across at least one monolayer of solvent, allowing the species to undergo redox reactions without directly interacting with the surface. The electrode transfer using a ruhex species is therefore highly insensitive to the electrochemical surface characteristics of the electrode.
By comparing the results obtained from these two species, we infer the specific effect of the electrochemical surface characteristics and kinetics of the electrode.

Electrochemical impedance spectroscopy

Electrochemical impedance spectroscopy (EIS) relies on the frequency behaviour of an electrochemical cell by applying an AC signal at a fixed potential or current to the cell and measuring the resulting response. Usually potentiostatic EIS is used at a constant potential. The electrochemical impedance characteristics can then be inferred from this response. EIS results are often shown as a Bode or Nyquist plot. The Bode plot is a combination of two plots which show the measured magnitude and phase at each frequency while the Nyquist plot shows the complex plane. The experimental response inferred from EIS can be fitted with an equivalent electrical circuit. The chosen circuit should be representative of the data obtained, but also based on previous knowledge of the physical makeup of the electrode in the electrochemical cell.

The simplified Randles circuit is the simplest circuit model of an electrochemical interface with a double layer as described in Section 2.4.2. The Randles circuit (illustrated in Figure 2.14) consists of an electrolyte resistance (R_S), a capacitator to characterise the double layer (C_{dl}), an active charge transfer resistance (R_{CT}) and a Warburg element (W). The Warburg element represents the diffusion of redox species towards the electrode. The semi-circle visible in the Randles circuit's Nyquist profile is indicative of the transfer resistance values. Larger circles indicate a higher transfer resistance. Sample conductivity also influences transfer resistance. A lower conductivity results in a larger transfer resistance. The semi-circle area is also indicative of the kintetics-controlled portion of the Nyquist plot. The straight line that ends the half-circle indicates the Warburg element (and thus diffusion) dominating the response instead of kinetics. For infinite or semi-infinite Warburg diffusion, the element is visible in the Nyquist plot as a straight line at 45 ° degrees phase between the element and the semicircle (which is observed as a 45 ° degree line from the real axis of the plot in most common scenarios). This behaviour indicates diffusion bound by a large planar electrode on one side. Mathematically, the Warburg element in these occasions is very close to a constant phase element (CPE) with a fixed phase angle of 45° degrees. These are sometimes used to model the Warburg element. The capacitor C_{dl} is often replaced by a constant phase element, which models the behavior of the double layer as an imperfect capacitor.
From the Randles circuit, certain characteristic coëfficients such as the transfer rate k_0 and diffusion coefficient D can be determined using the values derived from the EIS analysis.

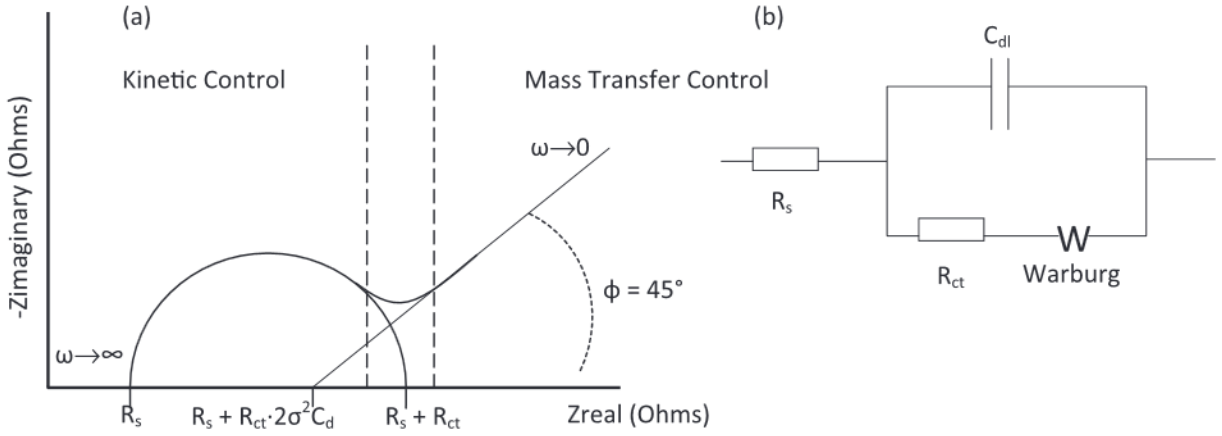

Figure 2.14: The Nyquist plot (a) and schematic circuit (b) representing a Randles circuit. Reproduced from Dornbusch et al. [49].

Another notable circuit (illustrated in Figure 2.15), applied to characterize certain BDD responses, is similar to one used to describe a polymer-coated metal surface [50, 51]. This circuit is used to detect defects and pores created by delamination of the thin film at the electrode surface. The elements in this circuit supplement the different versions of the Randles circuit commonly used. This circuit contains an added parallel circuit at the space normally occupied by the Warburg element in the Randles circuit. The parallel circuit consists of a resistance (R_{sp}), that is indicative of added solution resistance due to grain boundary

defects, and a CPE. This model is illustrated in Figure 2.15, with C representing C_{dl}, and Q the CPE.
The capacitance, shown as a characteristic half-circle in the Nyquist plot, can typically be attributed to sp^3 diamond, which has a chemically homogeneous surface and is associated with a single RC time constant. NDC impurities are highly disordered and contain sp^2 impurities, defects and high concentrations of boron dopant. These areas are heterogenous in multiple ways and cause a dispersed RC time constant. This is usually modeled using a CPE.
In this thesis, the Warburg element will be replaced with a CPE with an initial phase of 45 degrees for fitting purposes, and the double layer capacitance C_{dl} with a CPE to account for imperfection.

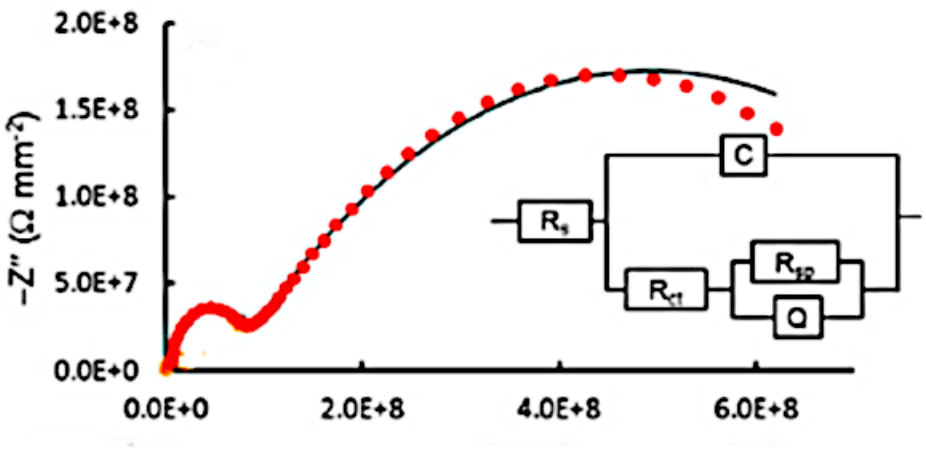

Figure 2.15: The Nyquist plot and schematic circuit representing the circuit similar to polymer-coated metal surface responses. Reproduced from Dutta et al. [50].

2.5 Nevirapine degradation and detection characterisation methods

2.5.1 UV-Vis Spectroscopy

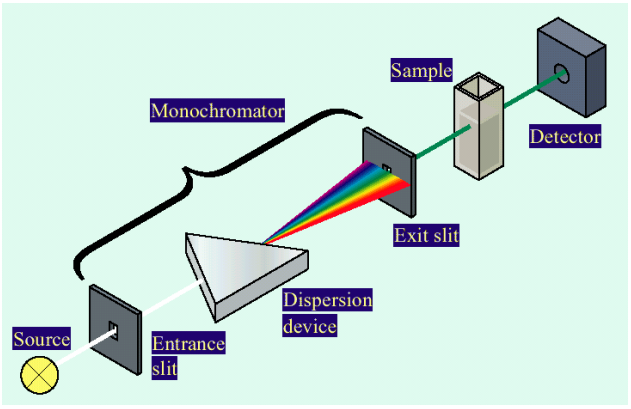

Figure 2.16: Schematical overview of the workings of a UV-Vis spectrophotometer from Shimadzu Scientific Instruments (SSI) [52].

Ultraviolet-visible spectroscopy (UV-Vis Spectroscopy) is a fast non-destructive analysis technique for analysis of compounds with pronounced absorption characteristics. The simplified basis of standard UV-Vis analysis relies on the interaction of electromagnetic radiation of specific wavelengths with molecules in a

dilute solution. A container containing a diluted compound is exposed to light from a certain wavelength filtered through a monochromator (as illustrated in Figure 2.16), which separates a single wavelength from the combined wavelengths of the source. It then passes through the container and is measured by a detector. When electromagnetic radiation hits a molecule in a solvent it can cause transitions to occur in the molecule. Depending on the energies involved, different transitions can occur. Within the ultraviolet and visible spectrum of electromagnetic radiation, these transitions are mostly limited to electronic excitation of bonding electrons. In this spectrum, the energy of the photon hitting the bonding electrons in a molecule can be equal to the transition energy needed to excite such an electron from an unexcited ground state into a higher energy orbital (excited state). If this occurs, the photon is absorbed to fuel this excitation. Transitioning from a ground state into the first excited state requires less energy than transitions into higher excitation states. Absorption at the transition from the ground state to the first excitation state is therefore stronger compared to transitions to higher states. Different kinds of bonds require different excitation energies. The structural features of a molecule that lead to absorption characteristics in the UV-wavelength of light are called chromophores in spectroscopy [53].
Due to this excitation effect, exposing a container of diluted analyte to a source of light with adjustable wavelength and measuring the light will result in a difference between emitted and detected light. The radiation exiting the fluid container (transmitted radiation) will be less than the radiation going in (incident radiation). This behaviour is influenced by the concentration of analyte molecules in the fluid and the path length. With higher concentrations molecules can be present in the "shadow" of each other. In these conditions, those molecules will not be hit by the radiation, which will make the measurement unreliable. In the range of concentrations in which no molecule is in the shadow of another, one of the practical expressions of the Beer-Lambert law applies (illustrated in Equation (2.8)). This expression relates measured absorbance (A) with c the molar concentration, ℓ the path length and ϵ the absorptivity or molar attenuation coefficient of the analyte.

$$A = \epsilon \ell c \tag{2.8}$$

This means that in concentrations with sufficiently low molarities, the measured absorbance will behave linearly. Within the range of this linear behaviour, the concentration of the analyte can be determined directly from the absorbance. To do this, selected characteristics of the UV response (such as preferably peaks in the response) are chosen and measured at different concentrations. For NVP, some important chromophores determining such responses are an $\alpha - \beta$ unsaturated ketone and a pyridine ring (observable in Figure 2.7)[54]. A wavelength where reproducible measurement for NVP concentration evaluation have been observed was 283 nm in acetonitrile:water (40:60 % v/v).
Standard UV-Vis spectroscopy is carried out by first creating a "blank", a reference signal composed of only the pure solvent (which together with the cuvette and air in the machine creates the ambient absorbance the signal needs to be compared to), and comparing it with a dilute solution of the sample species. Due to the interaction of the solvent with absorption, different solvents have different wavelength ranges in which they can be used. Water e.g. can be used for wavelengths down to around 190 nm. Due to the possible absorption of light by the container walls of the fluid container, the container materials also have a certain wavelength range in which they work. For UV analysis, quartz glass containers are the most prevalent due to their lower limit of around 170 nm for transparency purposes.

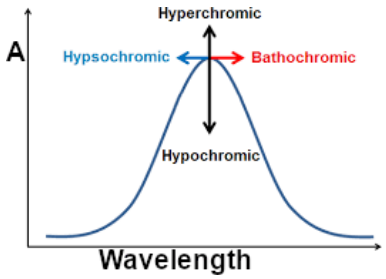

Figure 2.17: The different kinds of movements a peak in a UV spectrum can undergo.

Shifts in UV response are characterized differently as illustrated in Figure 2.17. When a characteristic

response shifts to a lower or higher wavelength (due to solvent differences or substitution), the shifts are called hypsochromic or bathochromic respectively. When an absorption intensity increases, it is called a hyperchromic effect, a decrease is called a hypochromic effect.

2.5.2 Differential Pulse Voltammetry

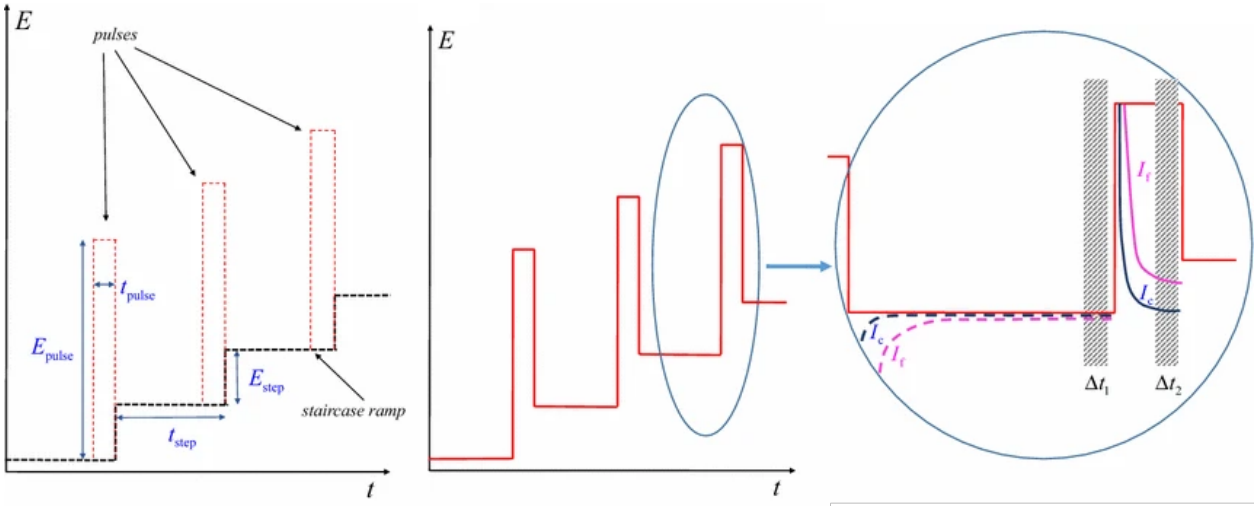

Figure 2.18: A DPV pulse staircase showing the essential pulse behaviour and the minimization of the capacitive current I_c. Adapted from Scholz [55].

Differential Pulse Voltammetry (DPV) is often used in NVP detection. DPV consists of potential pulses superimposed on a potential staircase ramp. During a DPV procedure, potential pulses are administered with a set pulse potential, pulse width and time frequency. After a pulse, the potential is returned to a settling potential that ramps up after each pulse with a set step size. This process is illustrated in Figure 2.18. Through DPV the current before a step can be subtracted from the current after a step. Each measuring point in a DPV graph will indicate the current difference between shortly before and at the end of a pulse. DPV allows measurements of electroactive compounds at very low molarities down to 10^{-7} to 10^{-8} M [55]. The resulting voltammogram takes a shape similar to a differential of the response that would be obtained in a normal CV or linear sweep procedure. It is however not a mathematical derivative of these procedures, but solely a graph of the differences between measured currents and applied potentials. The increased sensitivity compared to a normal CV or linear sweep is due to the minimization of capacitive current. The capacitive current is an interface effect of the electrode/electrolyte interface (the EDL from Section 2.4.2). This interface has two sides that can be charged and discharged like a condenser. However, these currents can interfere with the measuring of the currents used or generated when performing an oxidation or reduction reaction at the electrode (faradaic currents) [55]. When the potential or surface area on a capacitor changes a capacitive current will flow [56]. Since voltammetry relies on changing the potential, this effect is in play during ordinary CV procedures. This causes the noise and general size of the capacitive current to dominate the measured current behaviour when compared to the faradaic current, especially for solutions with a low analyte concentration. Since the capacitive current is independent from the analyte concentration, this decreases the sensitivity of the procedure, since lower analyte concentrations get drowned out by the capacitive current noise. Properly applied DPV avoids these interferences.

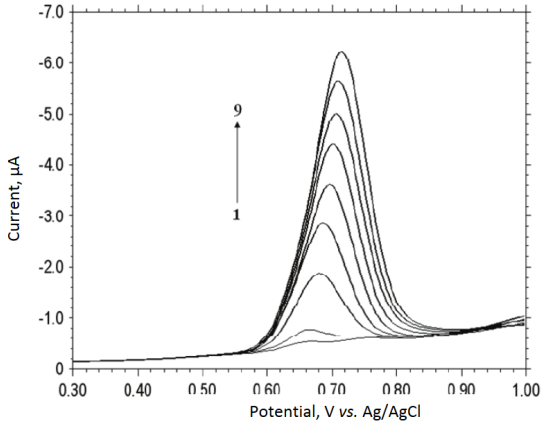

Figure 2.19: DPV's for increasing molarities of NVP in phosphate buffer (pH 10) at a GCE from 5 (1) to 350 (9) μM NVP reproduced from Teradal et al. [36].

With proper pulse width and pulse size, the effect of the capacitive current can be mitigated. DPV measurements for NVP as reported in Section 2.3.2 report a single peak around applied potentials of 0.6 - 0.8 V (illustrated in Figure 2.19). The NVP peak can also be obtained using CV, but the obtained response is lower and suffers from being harder to distinguish from the capacitive current.

Chapter 3

Research focus

The potential advantages of using boron doped diamond electrodes in the removal of micropollutants from wastewater are numerous. Pollutants require increasingly more attention as their scope and resistance to ordinary treatment procedures increase. Micropollutants are a class of pollutants whose resistance require processes such as electrochemical advanced oxidation to remove from the aquatic environment. Nevirapine is one such pollutant. Nevirapine is found in influent in wastewater plants in Africa, it is extensively used to treat HIV. The removal of nevirapine using BDD electrodes has not been attempted before, and could potentially provide a way to remove the pollutant from the aquatic environment. Detecting nevirapine using electrohcemical sensors is an established field with the aim to produce simple, cheap and sensitive sensors for routine anlysis in biological samples. The detection of nevirapine using BDD is novel and advantageous to consider due to BDD's low background current, robustness and biocompatibility, which promise a higher sensor lifespan and accuracy.
The different properties of the surface composition of BDD electrodes cause electrochemical differences between NCD and MCD diamond.
The core goals of this thesis are fourfold:

1. Characterise the surface of the BDD electrodes electrochemically and topographically.
2. Investigate the electrochemical degradation NVP using the BDD electrodes.
3. Study the electrochemical detection of NVP using the BDD electrodes.
4. Evaluate the performance of the BDD electrodes in aforementioned applications.

This thesis also aims to evaluate the condition of the electrodes after their use in the electrochemical experimentation. Research in the field of electrochemical advanced oxidation processes with BDD electrodes is relatively new for the diamond group of PME and research into nevirapine and nevirapine degradation is completely new to the group. Previous methods used have to be adapted and new methods to degrade substances have to be established.

Chapter 4

Experimental work

4.1 Boron doped diamond electrodes

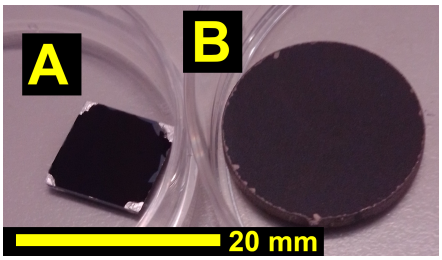

Figure 4.1: The Imec electrode sample (A) with silver paint applied to its corners for electrical connection, and the DiaCCon electrode (B)

Two different BDD electrode types were used in the experiments:
A NCD sample was obtained from IMEC, where a 4 μm thick film of highly-doped BDD was grown on a Si(100) wafer substrate using CVD. This electrode sample will be designated as the "Imec" electrode in this study. The Imec electrode was connected to the electrochemical cell using conductive silver paint, since the backside of this electrode was not conductive (see Figure 4.1).
The Imec sample was grown on a silicon (100) wafer substrate with a diameter of 200 mm, spin-seeded with 5 nm sized diamond nano-particles (NanoAmando aqueous colloid, NanoCarbon Research Institute) [41]. Seeding density was about 5x1010 cm^2. The seeded wafer was exposed to a CVD process in a hot filament chemical vapour deposition (HFCVD) reactor (sp^3 Diamond Technologies, model 655). Growth conditions were a mixture of hydrogen, methane and trimethylborane with ratios of CH_4/H_2 at 2.4 %, (72 sccm / 3000 sccm) , 40 sscm trimethylborane at 8 millibar pressure and around 850°C. Samples were produced from this wafer by carefully breaking the wafer mechanically.
A MCD electrode sample was obtained from DiaCCon GmbH where a 12 μm thick film was grown using HFCVD based on CH_4/H_2 chemistery on both sides of a niobium base using a 2000 °C filament and 800 °C substrate. One side of this sample was designated as the application side for use in experiments. This electrode sample will be designated as the "DiaCCon" electrode in this study.

4.2 Electrochemical cells

Two teflon cells were used in this thesis. These cells will henceforth be designated the "degradation cell" and the "detection cell"
The degradation cell was constructed according to the schematics seen in Figure 4.2. The electrode area exposed to the fluid is 22 mm^2 in diameter, and is protected from leaks using a Kalrez Compound 6375 O-ring. The electrode is clamped between this O-ring and a copper plate. Electrical connection between the copper plate and the electrode is either established through a normal contact interface with a BDD layer on the backside of the DiaCCon electrode, or on the Imec electrode through a cross-pattern of conductive silver paint. The open lid, sample holder and bulk material of the cell are teflon. The beaker was produced from a cylindrical piece of teflon.

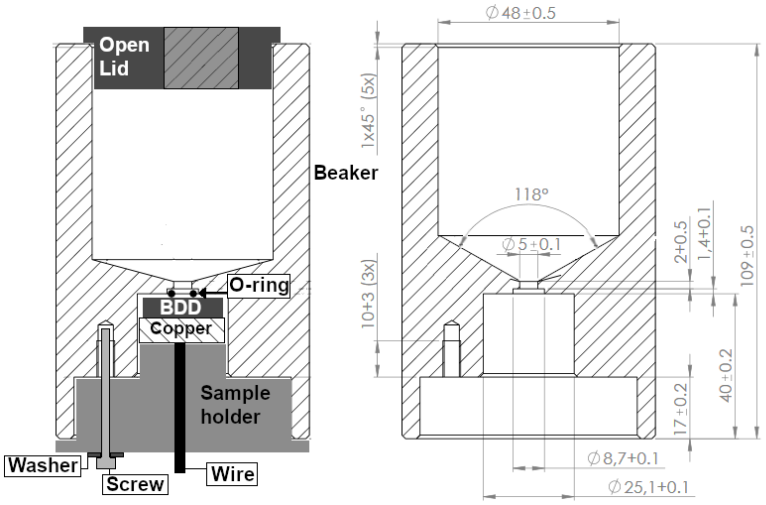

Figure 4.2: Assembly technical drawings of the electrochemical cell used to perform the degradation experiments.

The detection cell differs in having an inner angle towards the electrode of 150 degrees, and an exposed electrode surface area of 42 mm^2. The lid of the detection cell is flat, and does not have a hole to extract samples through. The counter electrodes in both cells are platinum wires of a length of 5.7 cm from BAS Inc., cat.no. 002222. The reference electrode used in both cells was an Ag/AgCl RE-1B Reference electrode from ALS Co., Ltd.
In between experimental procedures the cells were cleaned in a solution of $KMnO_4$ 1 g/l and H_2SO_4 0.1 M to remove potential leftovers from experiments.

4.3 Compounds

The water used in all of the electrochemical experiments and cleaning was $\sim$ 18 M Ω cm purified water from an ELGA PURELAB flex 4 water purification system [1].
NVP was acquired from Sigma-Aldrich in powder form, pharmaceutical secondary standard. An NVP stock of 190 μ M was made for the experiments. The solubility limit of NVP in water is 100 mg/l.
Supporting electrolytes used in the experiments were also obtained from Sigma-Aldrich in powder form, electrolytes were: phosphate buffered saline (1X) (PBS (1X)) [2] tablets, potassium nitrate (KNO_3) $\geq$ 99%, sodium sulfate (
The redox couples used were similarly obtained from Sigma-Aldrich in powder form. Ferrocyanide was obtained in the form of potassium hexacyanoferrate(II) trihydrate ($C_6FeK_4N_6 \cdot {}_3H_2O$) $\geq$ 99%. Ruhex in the form of hexaammineruthenium(III) chloride ($Ru(NH_3)_6Cl_3$) 98%.
Flasks used to prepare chemicals were specifically designated to be used for one solution type to prevent cross-contamination.

4.4 Electrode cleaning

Acid cleaning is highly recommended for diamond anodes [7]. Cleaning in boiling, concentrated sulfuric acid supersaturated with KNO_3 is recommended to clean the anode properly.
Acid cleaning was originally performed using sulfuric acid, nitric acid and KNO_3. The Imec anodes degraded very quickly in the acid cleaning procedure (illustrated in Figure 4.3), rendering it questionable to use them after three cleaning cycles. The heavy degradation visible in the SEM images would invalidate a comparison in electrode damage due to degradation or detection procedures. Ultrasonic cleaning at low intensity also

[1] When "water" is mentioned in the rest of this text, unless otherwise specified, assume it is purified water from this source.
[2] PBS (1X) consists out of 0.01 M phosphate buffer, 0.0027 M KCl and 0.137 M NaCl.

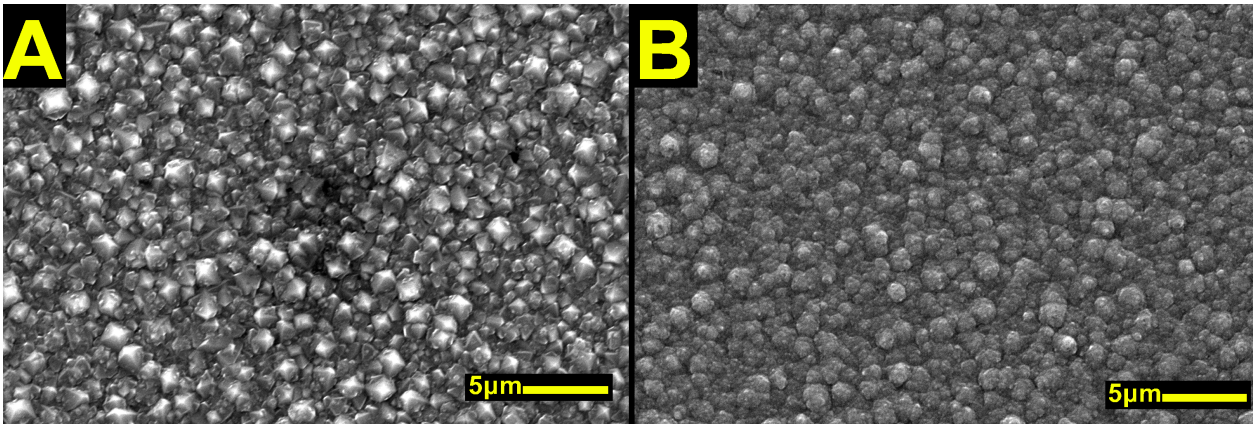

Figure 4.3: Representative SEM images of pristine (A) and three times acid-cleaned (B) Imec electrode sample surfaces

resulted in delamination of the film. Due to this drastic frailty, it was decided to clean the electrodes using a rinsing procedure of acetone and ethanol, with a distilled water rinse before and after every solvent rinse. To ensure comparative procedures among the electrode samples, this procedure was applied to both anodes.

4.5 Electrochemical characterization

Elctrochemical experiments were performed on a Metrohm Autolab Potentiostat (μ-AUTOLAB III) with eight M101 channels and a FRA2M impedance analysis module. Electrode characteristics analysis was done using the detection cell inside a Faraday cage (practical setup illustrated in Figure 7.9 in Chapter 7), using the working electrode area A = 0.416 cm^2. Ferrocyanide (1 mM) or ruhex (1 mM) with supporting electrolyte 0.1 M potassium nitrate (KNO_3). Prior to analysis, a reference experiment using only the supporting electrolyte was used. All solutions were bubbled with argon before measurement for at least half an hour to remove dissolved oxygen. For the redox behaviour, scan rates ranging from 0.025 to 0.8 Volt/second with doubling steps were chosen (0.025, 0.05, 0.1, 0.2, 0.4, 0.8). The step size used for these measurements was 0.01 V and the stop potential was 0 V. The range for the experiments was from -1 to 1 V for ferrocyanide experiments, and -0.4 to 0.1 V for the ruhex experiments. EIS was performed with 10 points per frequency decade, with a frequency range from to 10^6 to $0.1Hz$. The amplitude was 0.01 V and the maximum integration time was 0.125 seconds. The voltage setpoint for each of the experiments was chosen per experiment using the mean of all peak potentials to determine the formal potential [3]. Experiments were performed at room conditions ($20°C$, 293.15 K, standard pressure).
To analyse the results, an inhouse matlab script developed for previous work, kindly shared by Sartori et al. [41], Nova 2.1.3 and the open source matlab software ZfitGUI created by Jean-Luc Dellis were used. Nova was used to obtain an initial guess for the fitting process, which was manually improved upon using ZfitGUI's fitting system.

4.6 Degradation

Degradation experiments were performed in the degradation cell (practical setup illustrated in Figure 7.10 in Chapter 7). Each degradation attempt consists out of 1 hour of total degradation time divided in steps of 6 minutes. An 1 ml fluid sample was taken from the 80 ml total volume in the reactor at each interval, and at the end of the degradation. Each of these samples was diluted in a 1:10 dilution using water. During each 6 minute degradation step, the applied current and resulting potential difference were measured to track bubbling and potential problems. The current was selected at 0.0011 A (5mA/cm^2), a value that

[3]This was not done in the case of the ruhex measurement on the Imec electrode, which was kindly shared by Zhichao Liu and performed at a formal potential of 0 V.

was experimentally derived from preliminary degradation attempts in PBS (1X) as a rough current limit to prevent the excessive production of bubbles at the electrode surface. During degradation, overhead stirring was applied with a glass stirrer on 100 rpm.
Degradation was performed in different molarities of sodium sulfate (Na_2SO_4) and sodium chloride ($NaCl$). The molarity range investigated was 0.0039 M, 0.039 M and 0.39 M for both electrodes in both electrolytes. The NVP concentration of the degradation experiments was 95 μM.
Degradation attempts with the same electrolyte and BDD sample were generally performed on the same day. The attempts were arranged from low electrolyte concentration to high concentration, rinsing the cell three times with water between attempts.

4.6.1 UV-Vis analysis

Preliminary UV-Vis analysis on NVP concentration behaviour were performed on a Genesys 10S UV-Vis v4.004 using a 0.5 nm slit with a 0.1 nm interval on medium scan speed. Degradation analysis was done on a SHIMADZU UV-2600 UV-Vis Spectrophotometer using a 0.2 nm slit and a 1 nm interval. Quartzglass cuvettes were used with a path length of 10 mm. UV analysis was regularly done in the wavelength range from 185 nm to 400 nm, with some exceptions during the preliminary stages to check for eccentric behaviour outside of this range. The blank solutions used water in all cases.

4.6.2 Detection

DPV's were performed with the detection cell inside a Faraday cage using the Metrohm Autolab Potentiostat (practical setup also illustrated in Figure 7.9 in Chapter 7). The DPV procedures all included a range from 0 to 1 V with a 0.005 V step size, 0.05 V modulation amplitude, 0.05 seconds modulation time and a 0.5 second interval time. The final procedure settled upon was performed using 6 (4 in case of 50 μM NVP) regular DPV procedures as detailed followed by 4 DPV procedures preceded by an electrochemical activation step of -2V for 10 seconds.

4.7 Surface topography analysis

Scanning electron microscopy

SEM analysis before and after electrochemical experimentation of the two anode samples was done using a JSM-6010LA scanning electron microscope, at 15 keV. Observation was done on multiple spaces on the electrode before and after experimentation. Electrical connection was achieved using conductive adhesive carbon-tape. For the Imec sample the carbon tape was applied on the sides of the electrode so potential delamination would not destroy the electrode. For the DiaCCon sample the carbon tape was used on the non-application side of the electrode. Samples were cleaned before use using the same cleaning process as used in between electrochemical measurements.

Raman spectroscopy

Raman analysis before and after electrochemical experimentation was done using a Horiba Scientific Raman Spectroscope LabRAM S3000 running on Labspec using a 514.51 nm green Ar ion laser with a spectral resolution of ~ 0.3 cm^{-1}. Regular settings are: an acquisition time of 1 sec, accumulation of 1, either 50x or x100 objective, standard denoiser, 100 % ND Filter, 1800 grating, 1000 slit and 1000 hole. The temperature of the detector was reported at -132.91 ° C by the device during all measurements. Raman measurements on representative clean electrodes were made on multiple locations based on observed characteristic grain differences using the optical view of the spectroscope. Raman measurements on the electrodes after electrochemical experiments were made on representative areas previously exposed to fluid and areas outside of the area covered by the O-ring in the electrochemical cell. If presented as "noise-scaled", the Raman spectra obtained were scaled with their representative signal to noise ratio for illustration purposes, the background noise between 2000 and 3000 cm^{-1} was taken and compared to either the signal band of 1200 - 1300 cm^{-1} or the entire base of the characteristic peak around 1332 cm^{-} if present.

Atomic force microscopy

AFM analysis of the electrodes was done using a nanosurf AFM in air in room conditions.
A representative Imec sample electrode was analysed using a NCLR cantilever with an excitation amplitude of 1.9 V and no D gain, an I gain of 999 and a P gain of 10000 on dynamic force mode. Vibration amplitude was 200 mV with a setpoint of 55% and a vibration frequency of 166.446 kHz. The image size was 15μm x 15μm with a time per line of 998 miliseconds.
The DiaCCon sample was imaged using a CONTR tapping cantilever cantilever with a setpoint of 14.5 nN, no D gain, an I gain of 1500 and a P gain of 1000 on static force mode. The image dimension was 75.3μm x 75.3μm with a time per line of 998 miliseconds.
Post-processing and analysis was done in Gwyddion. Post-processing for both samples involved a level data by mean plane subtraction step to correct for slant.

Contact angle measurement

Contact angle measurement data was kindly shared by Diwakar Suresh Babu. These measurements were made using a Theta Lite Optical tensiometer with a droplet size of 3 microlitre. Measurements were done on both representative new electrode samples and the electrode samples used in the degradation and detection experiments of this thesis. Contact angles were fitted using a Young Laplace fit.

Chapter 5

Results and discussion

5.1 Surface characterisation results

5.1.1 Scanning electron microscopy

SEM imaging of DiaCCon BDD reveals primarily MC features of around 3 to 4 μm with irregular cubic facets and NC features near the grain boundaries. Clear crystalline features can be observed, which contrast to the much smaller grains in the Imec sample (with average sizes around 1 μm). The number of crystals seen is also lower, with less exposed grain boundaries. The Imec sample surface is primarily composed of NC features, with the larger exposed crystals jutting into the MC range. Both surfaces are as-grown, with crystalline facets increasing with growth time and consequentially film thickness. Representative SEM images of the two electrode surfaces can be seen in Figure 5.1.

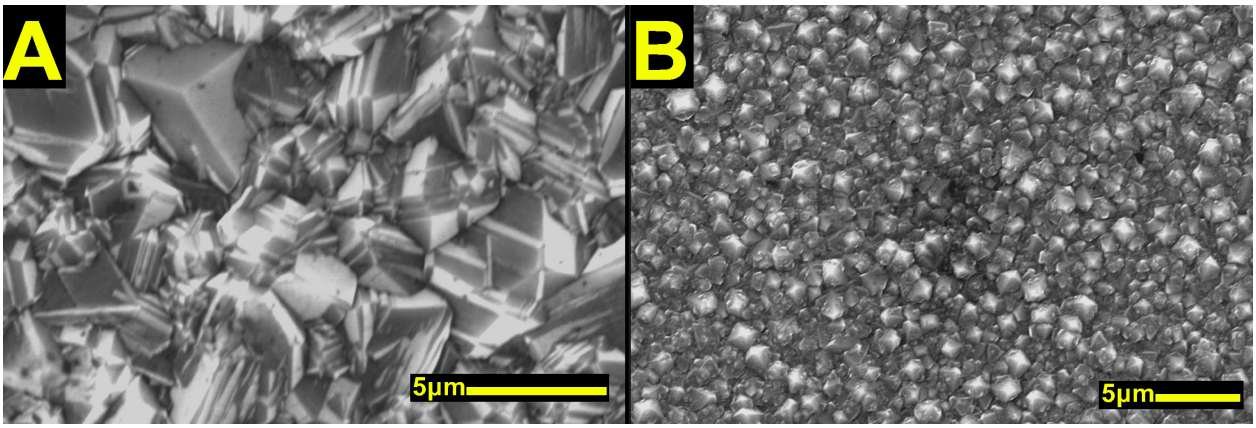

Figure 5.1: Representative SEM images of DiaCCon (A) and Imec (B) sample surfaces

5.1.2 Atomic force microscopy

After postprocessing the AFM images to correct for slanted surfaces, surface topographic data were derived (see Table 5.1). AFM reveals the topological structures identified in the SEM analysis (illustrated in Figure 5.2). Using the AFM derived root mean square roughness (DiaCCon 552 nm, Imec 263 nm), the observed effective surface area increase as opposed to a flat surface is derived for both electrodes. The effective increase between the two electrodes is extremely minor (i.e., about 18 % and 9 %, respectively) compared to the differences in composition. This suggests that observable differences in performance between the electrode are to be attributed to chemical composition of the electrode surface in contrast to a minor surface area increase due to MC/NC differences.

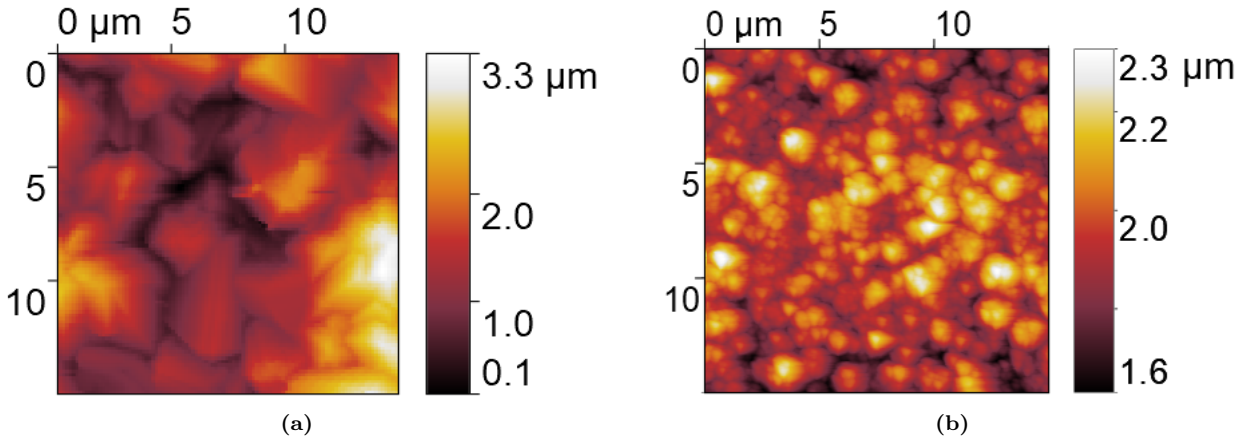

Figure 5.2: AFM topographic images of DiaCCon (a) and Imec (b) electrodes.

Table 5.1: Surface topographic data derived from AFM analysis

Sample:	DiaCCon	Imec
RMS roughness (Sq) [nm]:	552	263
Maximum height (Sz) [µm]:	4.00	1.36
Surface area/projected area [%]:	1.18	1.09

5.1.3 Raman spectroscopy

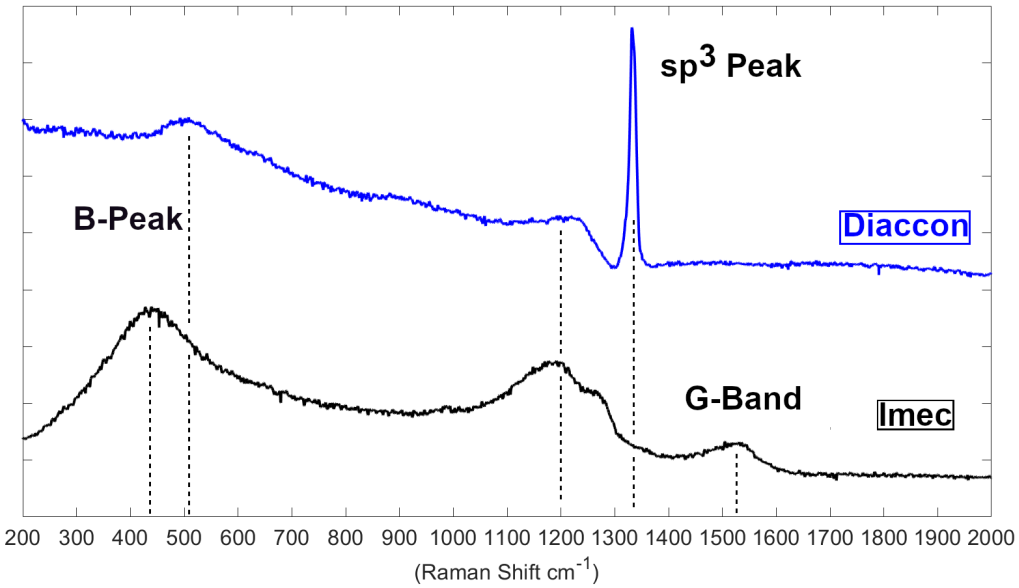

Figure 5.3: Noise-scaled representative Raman results obtained from the DiaCCon and Imec electrode samples.

Representative Raman spectroscopy results are illustrated in Figure 5.3. The DiaCCon sample has a large observable peak around 1332 cm^{-1}. This peak is attributable to the sp^3 carbon. The thin peak base (64 cm^{-1}) indicates a relatively high crystalline quality with few defects. This is likely due to the large MC features of the DiaCCon electrode BDD putting less grain boundaries in the laser spot. In comparison the Imec sample has two distorted branches around 1200-1300 cm^{-1} [41]. This is due to a Fano-type interference

commonly observed in BDD with metallic conductivity [7] and a side effect of high doping. Taking the peak intensity observed around 1270 cm^{-1} as indicative of the interfered sp^3 peak and comparing it to the intensity of the G- peak found at 1531 cm^{-1} and the background intensity at 2000 cm^{-1} , we get an estimated $\frac{sp^3}{sp^2}$ ratio of around 2.42. The DiaCCon $\frac{sp^3}{sp^2}$ ratio based on peak height is estimated to be around 22.8 using the 1332 cm^{-1} peak intensity, a similar background intensity at 2000 cm^{-1} and the intensity at 1500 cm^{-1} of the faintly observable G-band between 1400 and 1600 cm^{-1}. These ratios are to be taken as rough estimations, as the Imec sample has a sharp G-peak as opposed to the blunt and wide response in the DiaCCon sample, and the nature of the Fano-type interference requires a proper fit to be accurately gauged [57]. Both samples also have characteristic boron peak/band behaviour around 400 - 500 cm^{-1}.

5.1.4 Contact angle measurements

Contact angle measurement data shared as indicated in Section 4.7 reveals large angles on representative as-grown DiaCCon and Imec electrode surfaces. Contact angles were observed of around 71 ° for the DiaCCon electrode and around 82 ° for the Imec electrode, indicating more hydrophobic hydrogen terminated properties (as compared to a contact angle range of 0.6° to 65° degrees as indicated by Macpherson [7]). The Imec electrode appears to have a slightly more hydrophobic response (as illustrated in Figure 5.4 and Figure 5.5 in).

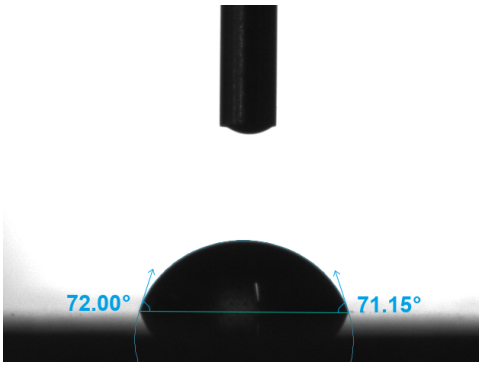

Figure 5.4: Contact angle measurement on a representative as-grown Diaccon electrode sample.

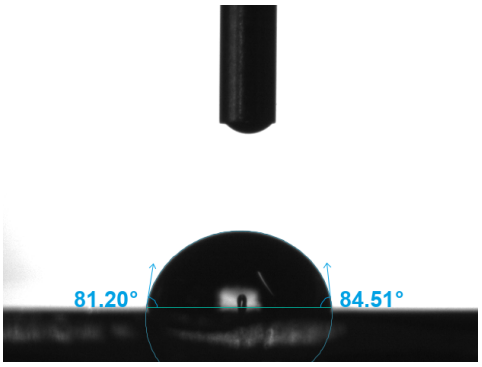

Figure 5.5: Contact angle measurement on a representative as-grown Imec electrode sample.

5.2 Surface characterisation discussion

The SEM and AFM analysis shows that the structure of the doped diamond anodes is markedly different, with previous studies suggesting MC and NC diamond have very different carbon makeups and electrochemical behaviour [7]. The obtained Raman spectra underscore the more disordered and amorphous nature of the Imec electrode as opposed to the DiaCCon electrode . The Raman spectra suggest that the Imec electrode is more heavily doped than the DiaCCon electrode. The comparatively larger boron related effects around 500 cm^{-1} and the distortion of the 1332 cm^{-1} peak into the behaviour seen around 1200 - 1300 cm^{-1} on the Imec electrode suggest heavy Fano interference [42]. The DiaCCon electrode also has a spectrum that can be compared to the onset of Fano type interference, demonstrated by a peak forming around 1230 cm^{-1}. This shows that both electrodes can be reliably interpreted as being heavily doped BDD electrodes. Raman analysis of the Imec electrode showed hugely similar results under all conditions, partly due to the surface topography being too small to focus on specific parts. Raman spectra of the DiaCCon sample do differ depending on the probed surface location, but all show similar characteristics. The intensity of the 1332 cm^{-1} peak fluctuates heavily here. The $\frac{sp^3}{sp^2}$ ratio observed in Figure 5.3 is cautiously taken at the lower end of the obtained results. The increased amount of grain boundaries observed on the Imec sample suggests more NDC in the Imec electrode. This indicates a larger background current in the Imec electrode, which could make it less sensitive in detection applications (assuming no electrochemical interaction occurs between NVP and

sp^2 carbon) [7]. Overall, the DiaCCon electrode sample shows a more pronounced $\frac{sp^3}{sp^2}$ ratio behaviour with the grain size and observed spectra favoring the DiaCCon electrode sample over the Imec electrode sample. This suggests that the DiaCCon electrode sample will perform favourably in degradation and detection applications compared to the Imec electrode sample. Contact angle measurements on representative as-grown samples show that the samples tend towards a hydrogen terminated surface, with a hydrophobic tendency.

5.3 Electrochemical characterisation

5.3.1 Potential window and background current

The potential windows for both electrodes were determined in 0.1 M KNO_3 at a scan rate of 0.1 V/s at a pH 7 after 20 minutes of argon bubbling. The range used was between -2 and 2.5 V. The tangent slopes of the OER and ORR reactions were used to determine the potential window.
The background currents were also determined from these voltammograms. The background currents read out after 10 scans for stabilization at 0.1 V during the forward scan were:

- DiaCCon electrode: potential window range of 2.66 V and background current of 6.3 $\mu A/cm^2$
- Imec electrode: potential window range of 2.48 V and background current of 31.2 $\mu A/cm^2$

The DiaCCon and Imec electrode share general behaviour and characteristics, both having wide potential windows and relatively low background currents. The DiaCCon electrode has a smaller background current in comparison to the Imec electrode, which conforms with previous assumptions derived from the $\frac{sp^3}{sp^2}$ ratio characteristics.

5.3.2 Ferrocyanide and ruhex

Measurements of the electrode kinetics in the presence of ferrocyanide and Ruhex redox couples are observable in Figure 5.6. Stabilization of the CV measurements was observed to initiate after roughly 5 scans, with 10 scans having negligible differences ranging in μA. Consequently the 10th scan of each scan cycle was used in determining electrode characteristics. The shape of the CV measurements conform to the known shapes of other CV measurements of these redox species on BDD [58][59].

Table 5.2: Redoxcouple results for the samples at a scan rate of 0.1 V/s at the 10th cycle in 1 mM ruhex or ferrocyanide.

Sample	Analyte	ΔE_p (mV)	Rct (Ω)	k_0 (μ m/s) Nicholson	k_0 (μ m/s) EIS
DiaCCon	$Fe(CN)_6^{4-}$	27.09	83	7.822	75.73
	$Ru(NH_3)_6^{3-}$	7.42	84	17.3	74.83
Imec	$Fe(CN)_6^{4-}$	10.13	41.8	56.7	150.39
	$Ru(NH_3)_6^{3-}$	7.11	– [a]	13.9	N/A

[a] A correct value could not be obtained as a result of a bad fit and corresponding model in the EIS results summarized in section 5.3.3

The ferrocyanide redox reaction appears to be more reversible on the Imec electrode with lower ΔE_p, which would indicate a higher k_0. The ruhex redox reaction appears to only have a minor peak current difference between the two electrodes. The ruhex measurements also show minor differences in ΔE_p when the scan rate changes, indicating quasi-reversible behaviour. The ΔE_p and k_0 values obtained through Nicholson's method for a scan-rate of 0.1 V/s are listed in Table 5.2.

5.3.3 Electrochemical impedance spectroscopy

EIS on both DiaCCon and Imec electrode surface (illustrated in Figure 5.7) shows a semi-half circle of kinetic behaviour in the ferrocyanide solution for both the DiaCCon and Imec electrodes. These regions appear

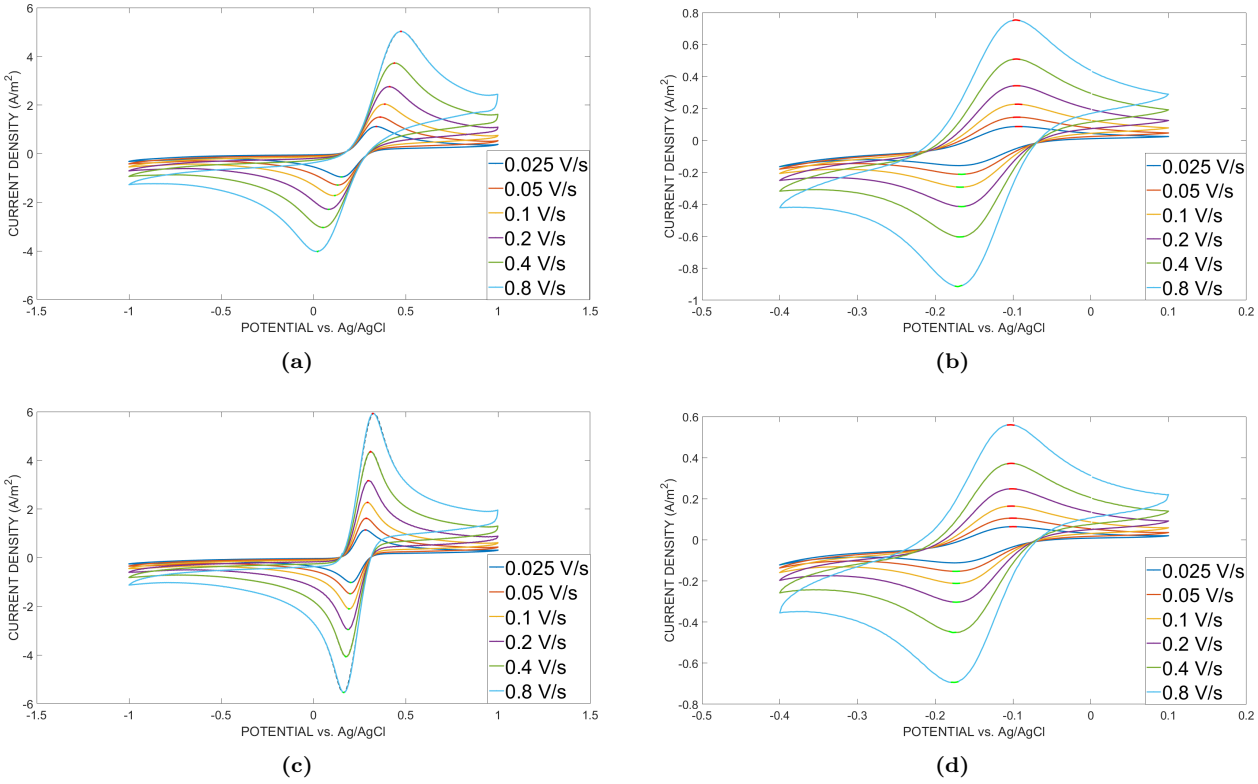

Figure 5.6: CV scan patterns obtained from redoxcouple measurements with 1mM ferrocyanide or ruhex in 0.1 M KNO_3, iR drop corrected. With (a): DiaCCon ferrocyanide, (b):DiaCCon ruhex, (c): Imec ferrocyanide, (d): Imec ruhex.

largely similar. For the kinetic behaviour in the ruhex, a section of the characteristic half-circle is observed at high frequencies, which is followed by a large upwards line for both electrodes which dominates the response and extends very far from the ferrocyanide regions (this can be observed by comparing Figure 5.7 to Figure 5.10 and Figure 5.11). In the ferrocyanide response, at lower frequencies, the response straightens into a 45 ° angle for both samples, which is indicative of a diffusion dominated response which can be modelled using a Warburg element or replacement CPE. The obtained responses show complex behaviour compared to the original models discussed in Section 2.4.2. Primarily, the response of the DiaCCon circuit closely resembles the alternative circuit investigated for MC BDD used in Section 2.4.2, but expanded beyond the scope of the original circuit. The response obtained on the Imec sample in ferrocyanide also contains an additive element between the characteristic semi circle and 45 ° angle, which slightly extends kinetic behaviour.

As a fit is only as good as the model it uses can allow, it is important to discuss the model used before continuing into results. The model used to fit the DiaCCon electrode sample was the extended model shown in Figure 2.15 and described in Section 2.4.2. The Imec electrode sample was fitted using the Randles circuit instead. Fits for both the ferrocyanide responses can be seen in Figure 5.8 and Figure 5.9. Both fits fail to capture the diffusion dominated region, and the Warburg element is not captured in both circuits. In the DiaCCon response, the Warburg element is not incorporated as part of the model, and the model would require an addition to model it properly. In the Imec response, the fit and model cannot properly deal with the added region of kinetics in-between the semicircle and diffusion dominated region.
Where the responses obtained in ferrocyanide are still representative of elements of the models applied, the ruhex responses obtained were completely dissimilar. The Ruhex responses still share a part of the semicircle the ferrocyanide responses both have, but these regions are distorted and feature loops (illustrated in Figure 7.8 in Chapter 7). The circuit models applied do not properly model or reflect this behaviour, and the EIS results from the ruhex experiments should therefore be distrusted accordingly. The ruhex

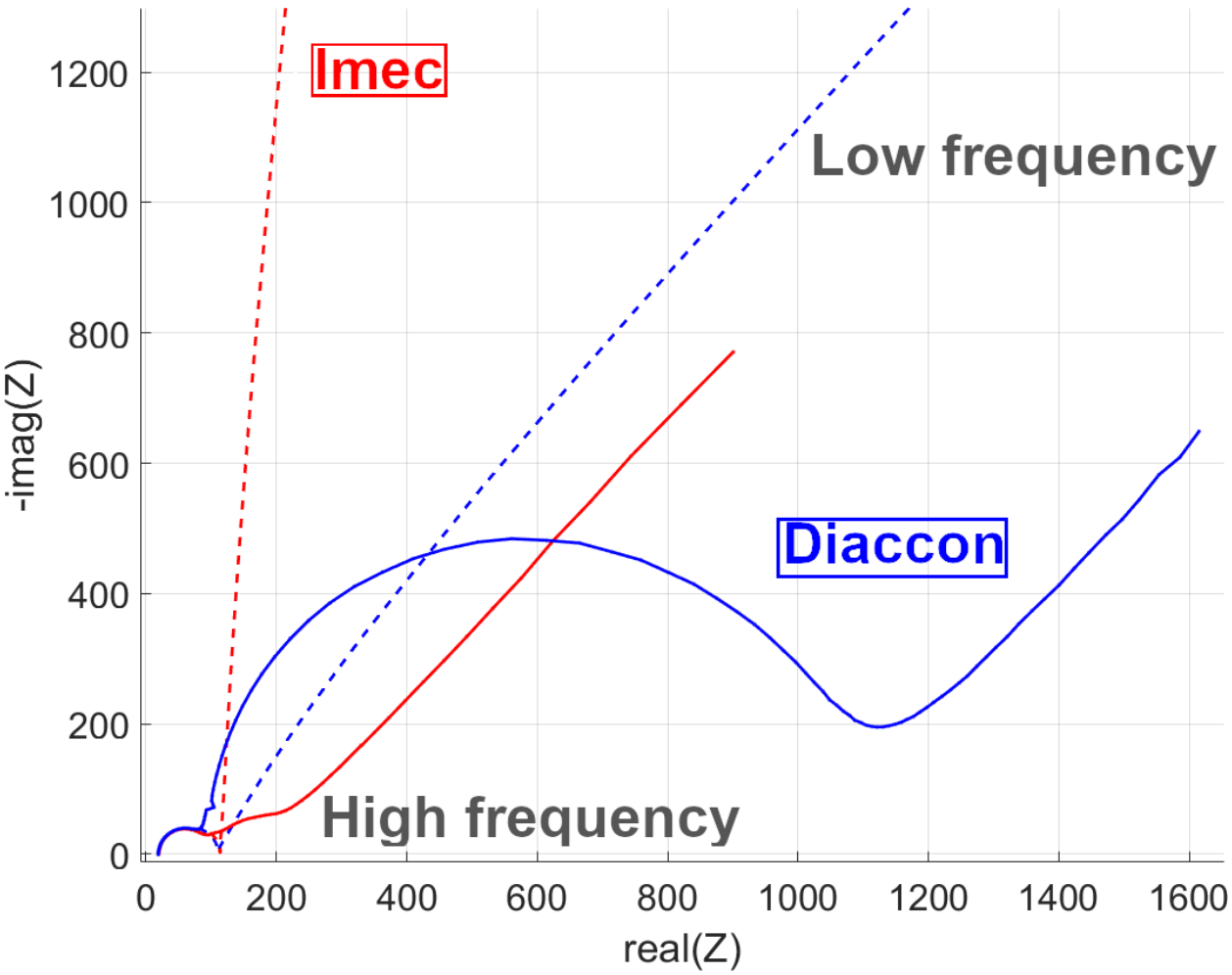

Figure 5.7: EIS results of the DiaCCon and Imec electrodes using 1mM ferrocyanide (solid lines) or 1 mM ruhex (dashed lines) in 0.1 M KNO_3 using a frequency range from to 10^6 to $0.1Hz$ and an amplitude of 0.01 V at the formal potentials.

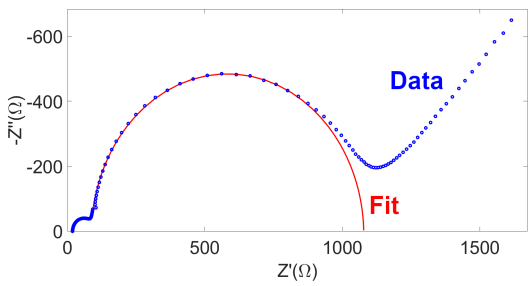

Figure 5.8: EIS fitting results obtained using the DiaCCon electrode sample in 1mM ferrocyanide

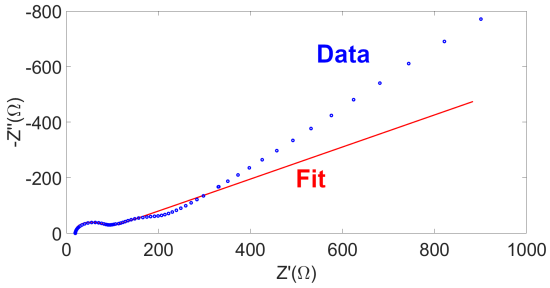

Figure 5.9: EIS fitting results obtained using the Imec electrode sample in 1mM ferrocyanide

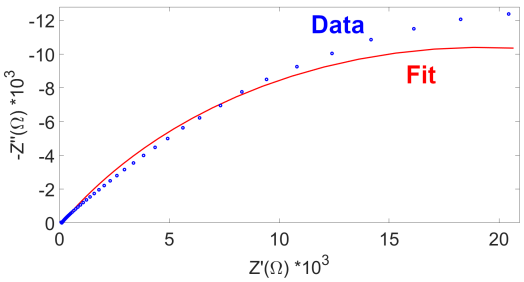

Figure 5.10: EIS fitting results obtained using the DiaCCon electrode sample in 1mM ruhex

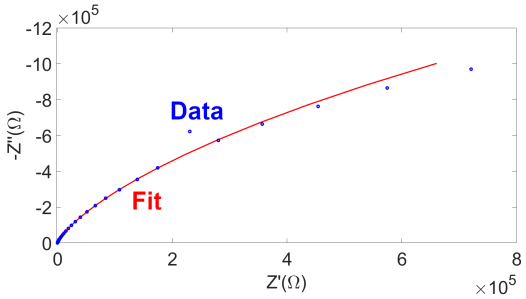

Figure 5.11: EIS fitting results obtained using the Imec electrode sample in 1mM ruhex

responses do share similarity on high frequency, indicating that the kinetics between the electrodes are not that different with an outer-sphere transfer. The model parameters from the resulting fits show significant deviation however, with the R_{CT} being around 84 for the DiaCCon electrode sample in both the ferrocyanide and ruhex while the Imec electrode sample has drastically differing values while still exhibiting the same behaviour. This is partly due to the fitting problem with the chosen model and data.
The representative circuit data obtained is listed in Table 7.1 and Table 7.2 in Chapter 7. The resulting R_{CT} and k_0 are listed in Table 5.2.

5.4 NVP UV-Vis results

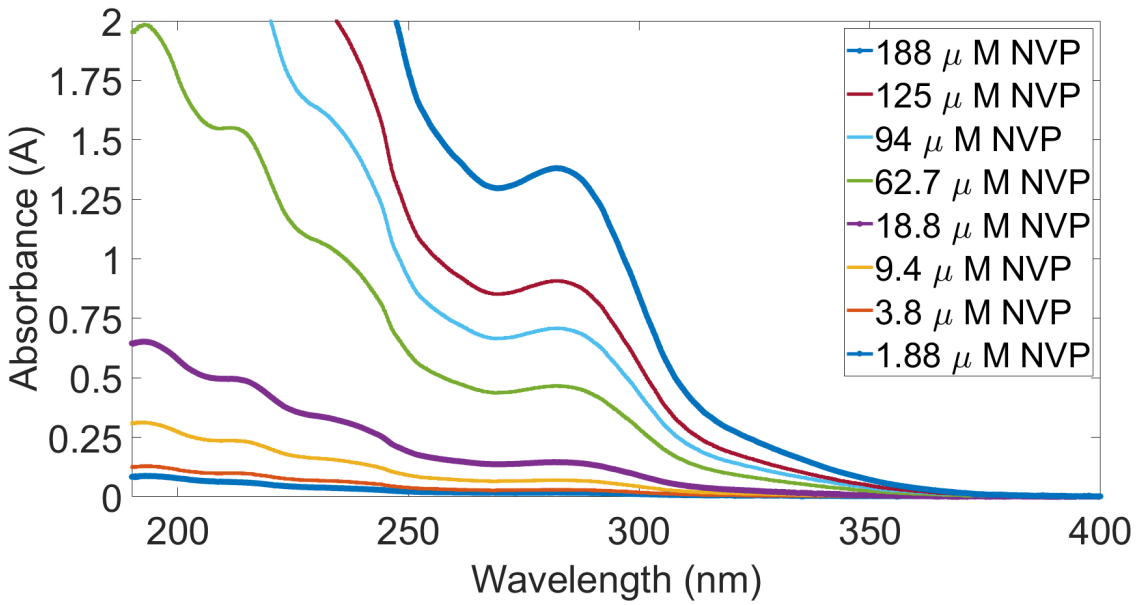

Figure 5.12: UV spectrophotometry results of different NVP molarities in a range from 1.88 to 188 μM.

Nevirapine concentrations were investigated in water reflecting a log scale of 1.8, 18 and 188 μM NVP, with the characteristic response being a pronounced peak at a wavelength of 282 nm. Using a least-squares method fit, a linear regression was made of the absorbance measured at the observed 282 nm peak. The regression formula, Equation (5.1) (with the concentraction ($conc_{NVP}$) and in μM) , was fitted with a root mean squared error of 0.014, and standard errors of $6.73 * 10^{-3}$ for the intercept and $5.4 * 10^{-5}$ for the slope.

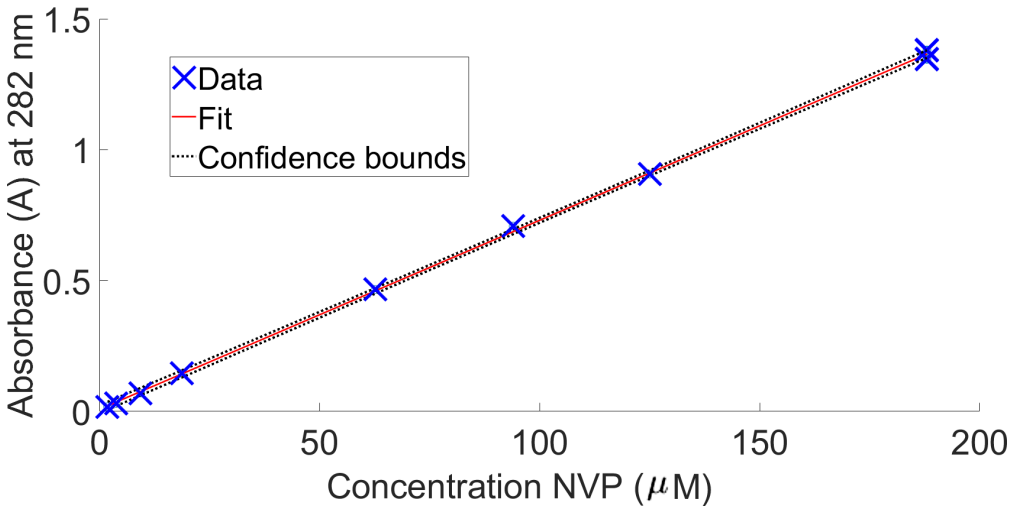

Figure 5.13: Linear regression of the peak response at 282 nm of dissolved NVP compared to water.

$$A = 0.008 + 0.007 * conc_{NVP} \tag{5.1}$$

A representation of the linear regression and peak data points can be seen in Figure 5.13. The range in this study (from 1.8 to 188 μM) is semi-quantitative, as it does not satisfy Beer-Lambert linearity, which requires a higher degree of confidence. The linear range for NVP has in previous instances been found to be aproximately 1-5 $\mu g/ml$ (around 3.8 - 19 μM) in mixtures of water and methanol [60].

5.5 Electrochemical degradation results

Degradation was attempted in different molarities of sodium chloride and sodium sulfate. Minor bubble formation at the WE was observed in all cases. Potential resulting from the current difference varied with increasing molarity and therefore increasing electrolyte conductivity. The UV-Vis response observed from NVP after degradation using BDD and a current of 5 mA/cm^2 turned out different between electrolytes and electrodes. Degradation attempts in lower concentrations of electrolyte (0.0036 M NaCl or Na_2SO_4) show no discernible changes in UV profile, while attempted degradation at higher concentrations do show differing behaviour.

5.5.1 UV-Vis spectrophotometry results

Sodium Sulfate

A lowering of absorbance in the UV-Vis spectrum is observed using the DiaCCon electrode in 0.39M Na_2SO_4 at all wavelengths. The effect observed is illustrated in Figure 5.14. The spectrum retains the characteristic profile of NVP, and peak height at a wavelength of 282 nm can be tracked as a quantative indication of NVP concentration.
Tracking the lowering of the peak wavelength at 240 nm, the absorbance decreases at the sample taken at 6 minutes, but stabilizes afterwards, and stays stable for the subsequently measured samples. The total absorbance lowering observed is 0.013 A, which using Equation (5.1) and the dilution factor of $\frac{1}{10}$ would roughly indicate a decrease of around 19 μM. This change seems inhibited after the first 12 minutes of applied current.
Degradation attempts in Na_2SO_4 on other electrodes and molarities did not result in a measurable UV-Vis difference large enough to avoid being mere noise (e.g. differences of 0.001 A).

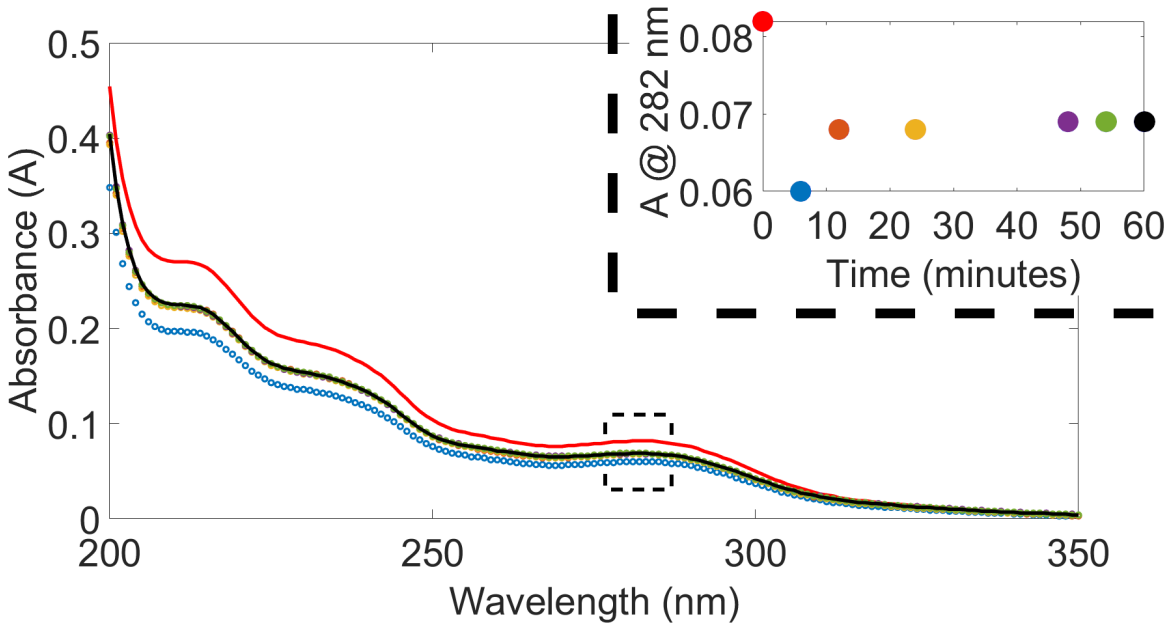

Figure 5.14: UV spectrophotometry results of both the general profile and the lowering of the absorbance intensity of the peak at 282 nm.

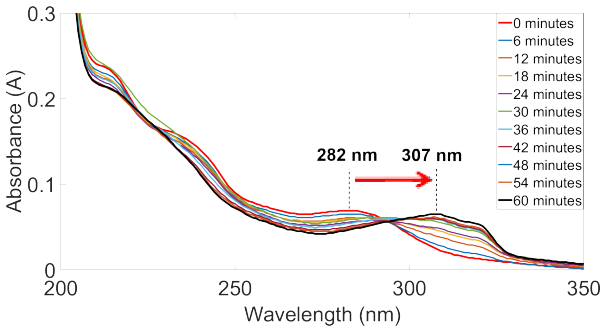

Figure 5.15: NVP UV-Vis response behaviour on the DiaCCon electrode during attempted degradation in 0.39 M NaCl.

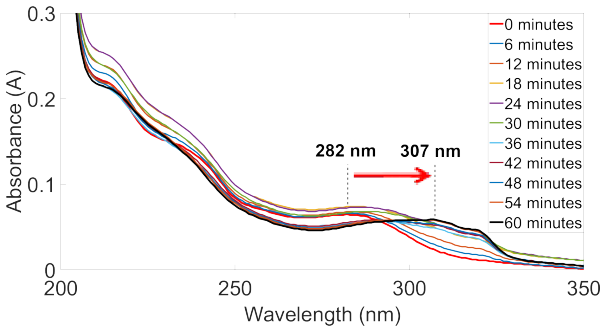

Figure 5.16: NVP UV-Vis response behaviour on the Imec electrode during attempted degradation in 0.39 M NaCl.

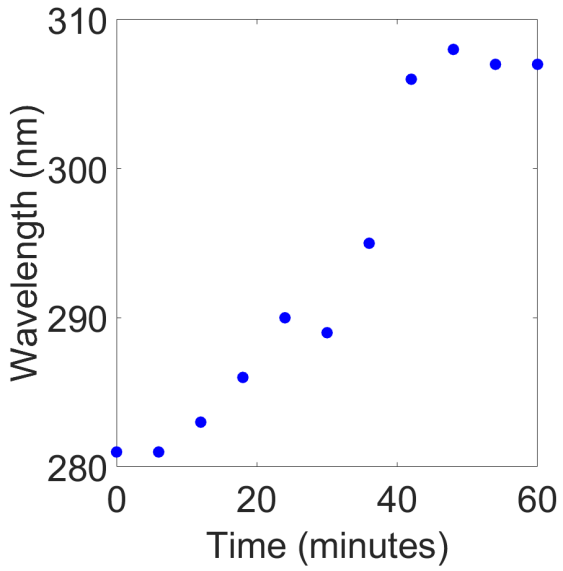

Figure 5.17: Bathochromic movement of the characteristic NVP peak on DiaCCon electrode during attempted degradation in 0.39 M NaCl.

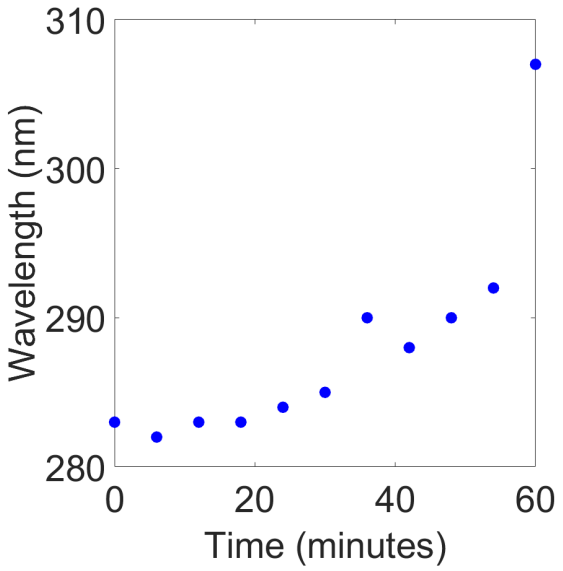

Figure 5.18: Bathochromic movement of the characteristic NVP peak on Imec electrode during attempted degradation in 0.39 M NaCl.

Sodium Chloride

Degradation attempts in NaCl reveal markedly different behaviour in comparison from Na_2SO_4, illustrated in Figure 5.15 and Figure 5.16. At higher concentration levels, a peak shift occurs where the peak originally at 282 nm shifts towards longer wavelengths, a bathochromic shift. At the regions of the UV-profile with a wavelength lower than 250 nm, a generally hypochromic intensity lowering shift is revealed. This behaviour was observed on both the DiaCCon and Imec sample at molarity levels of both 0.39 M, and signs of a trend towards these changes were perceivable at 0.039 M for both electrodes, although not quantifiable to a high enough degree to compare. The bathochromic shift after an hour with the DiaCCon electrode in 0.39 M settles at around 54 minutes and the peak ends up on a wavelength of 307 nm. With the Imec electrode sample, the bathochromic shift of the peak ends up on 307 nm as well, but less timely, only just arriving at the end. The peak absorption intensity fluctuates slightly during this process, making a slight hypochromic movement downwards before rising back up on the DiaCCon electrode while doing the reverse on the Imec electrode, starting off with a hyperchromic trend. Both eventually trend back towards a value around the original peak intensity. Graphical presentations of the bathochromic shifts in characteristic peak location over time are illustrated in Figure 5.17 and Figure 5.18.

5.5.2 UV-Vis spectrophotometry results discussion

The quick lowering of the absorption profile at the DiaCCon electrode in 0.39 M Na_2SO_4 but subsequent non-activity suggests the observed activity is not the result of a classical degradation profile. Degradation of micro-pollutants in literature shows that under normal conditions, degradation should be spread out over time, with changes that gradually level off over time. Comparatively the changes seen in Na_2SO_4 are not reliable or indicative of degradation. Apart from a possible mismatch in the NVP level obtained from the initial conditions measurement, the absorbance levelling off after 12 minutes at 5 mA/cm^2 indicates a fast process that stops immediately. The breakdown of NVP would require intermediate products with different UV-Vis behaviour due to the breakdown or conjugation of chromophores. This renders the results obtained in Na_2SO_4 non-indicative of NVP degradation.
The degradation attempts in NaCl show different behaviour, with the characteristic peak at 282 nm shifting to higher wavelengths and the absorption intensities between 200 and 250 nm lowering. These changes, observed together as a shared process, suggest slight changes in the NVP molecule, such as the potential

attachment or detachment of functional groups which result in a higher peak response. The attachment or replacement of atoms in chromophores result in changes in absorption intensity and characteristic peak. Overall, the behaviour observed in NaCl is indicative of minor changes in the NVP molecule, but it does not provide indication for any full degradation or breakdown of the molecule. Mineralization of NVP into simple inorganics (e.g. CO_2 or H_2O) would require UV spectra exhibiting major shifts. If the observed behaviour would be indicative of degradation however, the responses obtained in NaCl would have to share similarities to the responses obtained in Na_2SO_4. The main difference between the electrolytes is the generation of sulfate radicals and persulfate or active chlorine and reactive chlorine species [61]. This suggests the presence of chlorine in the solution allowed reactions which affected the NVP. Degradation of the substance by these chlorine induced reactions cannot be confirmed from this response. Hydroxyl radicals should be readily produced in both solutions as the measured applied potential difference during degradation exceeded the required potential for the generation of hydroxyl radicals (1.23 V vs standard hydrogen electrode RE, which is around 1.28 when using a Ag/AgCl RE) [62].

The degradation of NVP cannot be confirmed from these measurements alone, though the *complete* lack of degradation cannot be confirmed either. The responses obtained in NaCl suggest a more specific reaction related to chlorine such as chlorination of the NVP compound. NVP's chlorination in high levels of chlorination inducing substances and nevirapine oxidation by NaOCl in different conditions was tested previously in research by Wood et al. [29], and electrochemical formation of active chlorine and reactive chlorine species in a high molarity NaCl solution represents similar levels of chlorinating power. While the chlorination of NVP may eventually break down the product, it is ismpossible to quantify this change using UV-vis measurements alone. Further investigation into the behaviour of NVP in EAOP involving chlorine will have to be conducted using a method that can detect and classify chlorinated NVP compounds.

5.6 DPV results

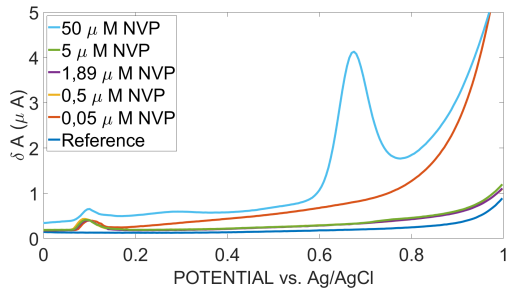

Figure 5.19: NVP response for the first DPV performed in different NVP molarities on the DiaCCon electrode in PBS (1X)

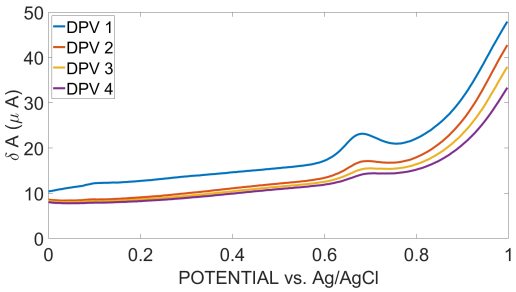

Figure 5.20: NVP response behaviour on the Imec electrode decreasing in response to repeated DPV measurements in 50 μ Molar NVP in PBS (1X)

DPV measurements of NVP on DiaCCon and Imec electrodes in PBS (1X) at pH 7.4 using a range (0.5 to 50 μM) shows several characteristic behaviours throughout preliminary testing and actual experimentation:

- DPV's in NVP solutions at high molarity (50 μ M in Figure 5.19 and Figure 5.20) show peaks around the applied potentials 0.67 V. In PBS (1X) an additional peak is found near 0.1 V which does not correlate with the molarity of NVP in the solution.
- Response behaviour requires a relatively high concentration of NVP (e.g. 50 μ M).
- DPV response at the applied potential around 0.67 V decreases with each recorded DPV (illustrated in Figure 5.20)

- Responses on the DiaCCon electrode sample occupy a lower current difference scale compared to the responses on the Imec electrode sample. (e.g. current difference (δ A) at an applied potential of 0.2 in reference solution are around 0.13 and 8.2 δ μA for respectively DiaCCon and Imec responses.)

Observed peak values for NVP on DiaCCon and Imec electrode samples in 50 μ M are listed in Section 5.6.

Table 5.3: Current peaks associated with NVP response in 50 μ M NVP.

Electrode sample	DPV order	NVP Peak current ($\delta\mu A$)	Peak potential (mV vs Ag/AgCl)
DiaCCon	1	4.1	675
	2	2.1	685
	3	1.5	700
	4	1.1	710
Imec	1	23.2	680
	2	17.1	685
	3	15.5	700
	4	14.4	705

5.7 Discussion of DPV results: observed behaviour and detection inhibition by NVP.

The peak observed around 0.67 V in DPVs on a range from 0 to 1 V in (50 μ M) is within a range (0.6 - 0.8 V applied potential) observed within previous NVP detection studies as recorded in Table 2.1 in Section 2.3.2. The oxidation process of NVP was also found to be irreversible in these studies. The peak found in 50 μ M NVP on the DiaCCon electrode (see Figure 5.19) appears more pronounced compared to the peak observed on the Imec electrode. The higher range of the current difference is an effect of the capacitive behaviour of the electrode surface. The capacitive current on the Imec electrode is observed to be larger than the capacitive current on the DiaCCon electrode.
The decreasing response with each DPV applied (illustrated in the behaviour exhibited in 50 μ M, see Figure 5.20) suggests that repeated NVP oxidation is inhibiting the electrode. This is supported by the change in observable baseline and starting point between the reference DPV's and NVP DPV's. As DPV relies on reducing the capacitive current, a change in capacitance due to e.g. fouling/inhibiting of the electrode will change the DPV results. Smooth baselines with consistent noise behaviour but strange offsets suggest a change in the surface of the WE in contrast to a fault in the RE. A change in the RE would result in a very noisy signal with discontinuities due to the lack of proper potential difference measurement. This has not been observed. Another potential inhibiting effect would be the interaction between NVP and different surface terminations of BDD such as adsorption on the electrode or interactions dependent on the termination of the electrode.

Adsorption of NVP or its oxidation products on electrode surfaces has been reported at GCE electrodes by Teradal et al. [36], using multiple CV sweeps to show a significant decrease in peak current. High end NVP sensing as listed in Table 2.1 in Section 2.3.2 use techniques that avoid adsorption directly on the electrode surface such as absorptive stripping using mercury or the addition of functional groups on the electrode surface. Examples include using uracil on a CPE [30] or Bi_2O_3 on a CPE [20] to enhance electrocatalytic activity towards NVP oxidation. The observed behaviour in repeated DPV sweeps in the same solution suggests that, despite BDD's comparatively advantageous properties in fouling resistance, adsorption based NVP fouling still occurs. The observed detection results are therefore suspect, as the state of fouling after degradation experimentation but prior to detection experimentation cannot be accurately gauged. This turns any attempt to tune the DPV parameters into a laborious and unreliable procedure. To avoid having the observed behaviour and potential fouling remnants meddle with detection results on BDD electrodes, two methods were discerned as potentially applicable.

1. Clean the electrodes before and after each individual DPV measurement, using acid treatment as outlined in Section 4.4.

2. Attempt to use *in-situ* electrochemical activation to recover NVP detection.

Both of these methods have advantages and disadvantages:
Cleaning the electrodes with acid before each measurement would provide accurate and consistent detection results, but would require an unfeasible amount of time due to the tuning required to perform satisfactory cleaning while not destroying the Imec electrode sample as observed in Section 4.4.
Electrochemical activation could in contrast be applied during the DPV measurements, but might not fully recover peak response behaviour. This process requires optimization to adjust to the conditions on the electrode surface, but can offer stability for repeated measurements. There is no previous literature on in-situ electrochemical activation or electrochemical pretreatment for NVP detection on BDD electrodes. Electrochemical activation (particularly in-situ) is easy to apply, requiring only a simple addition to the program structure used for DPV experimentation. Electrochemical activation is therefore both quicker, and potentially interesting to stabilize the responses in preparation for tuning. Electrochemical activation is not without risks, as the process relies on an over-potential which could damage the electrode. However, BDD has the ability to endure extreme potentials, making the procedure relatively safer on BDD compared to other electrode materials.
It should be noted that both procedures also affect the termination of the BDD surface. Acid cleaning in boiling acid in particular is often recommended to induce oxygen terminated surface [7]. While acid cleaning would remove any potential leftover NVP adsorbed to the surface, it would also induce oxygen termination. In-situ electrochemical activation has the potential to recover hydrogen termination on BDD electrodes [63]. Representative as-grown DiaCCon and Imec electrode samples show significant hydrogen termination tendency, which could potentially have been reduced during degradation procedures. The preference of NVP detection procedures for hydrogen or oxygen terminated BDD was not recorded in literature.
With these considerations, electrochemical activation was implemented in this study to combat the inferred electrode fouling by NVP.

5.8 DPV results using in-situ electrochemical activation

Electrochemical activation in detection applications is a process intended to clean an electrode surface. The base process involves the use of cathodic and/or anodic potentials or pulses. The process can remove adsorbed material or even a thin surface layer of the electrode surface itself. Generally, this is done by pulsing the electrode with a relatively high or reversed potential to drastically affect the surface chemistry. Electrochemical activation can be employed to try and directly oxidize or reduce fouling agents, or dislodge them using the products from either the anodic or cathodic reactions available. Furthermore, electrochemical activation on BDD surfaces can yield changes in surface termination, or damage [64]. Cathodic activation in H_2SO_4 has been used to increase hydrogen termination on BDD electrodes [13, 65]. In-situ electrochemical activation of BDD using a set pulse behaviour has been successfully applied to recover signal loss due to fouling [63]. Anodic or cathodic pulses have been applied in different setups. Due to NVP's observed behaviour under oxidation and the observed lack of degradation, in-situ cathodic electrochemical activation was selected as a recovery procedure.
In this study detection was performed using 6 (4 in case of 50 μM NVP) regular DPV procedures followed by 4 "activated" DPV procedures. Each "activated" DPV procedure was preceded by an in-situ electrochemical activation step, by applying a controlled -2 V potential for 10 seconds (cathodic activation).
Peak behaviour was recovered after applying electrochemical activation. Even in cases where the peak response of NVP had decreased beyond discernible boundaries (e.g. Figure 5.21), peak behaviour was recovered after cathodic activation (e.g. Figure 5.22).
The baseline currents observed after cathodic activation were higher compared to inactivated DPV responses. This effect was also observable in a reference solution without NVP. This effect is most likely due to the changes induced in the surface during the electrochemical activation process.
Quantification of the detection of NVP is still obstructed by the changes in baseline between scans. The classic signal to noise ratio (SNR) measurement in electrochemistery is based on the standard deviation of a reference signal compared to the peak height of the characteristic response. Unfortunately, the electrochemical response has to be properly tuned to result in a correct assessment, which requires further study.

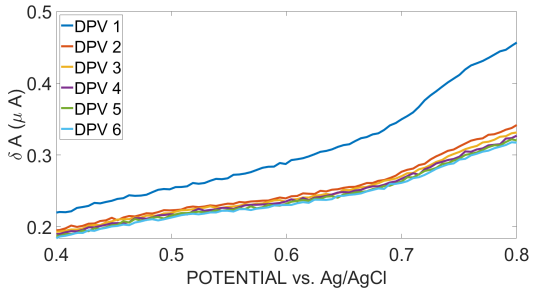

Figure 5.21: A cutout of the DPV responses measured prior to cathodic activation on the DiaCCon electrode in 5 μ Molar NVP in PBS (1X)

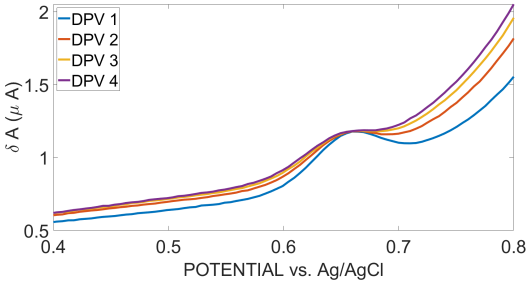

Figure 5.22: The NVP response obtained on the DiaCCon electrode directly after the measurements shown in Figure 5.21 using DPVs preceded by in-situ cathodic activation.

An estimated attempt was made to establish the limit of detection (LOD) and limit of quantification (LOQ) using an adaptation of the method used in the study by Teradal and Seetharamappa [20].
For this method, using the peak heights observed at different molarities, assuming a linear response holds, the different peak heights can be fitted by linear regression. The slope of this regression then relates to the LOD and LOQ as seen in Equation (5.2) and Equation (5.3) where σ is the standard deviation measured in the blank and m is the slope of the linear regression.

$$LOD = 3 * \sigma / m \tag{5.2}$$

$$LOQ = 10 * \sigma / m \tag{5.3}$$

It should be noted that the ordinary minimum reference measurements recommended to get a proper standard deviation are 10 instead of 4. There are not enough measurements present to guarantee a linear response within the investigated NVP molarities [1], with only a minor amount of detectable peaks at different molarities in the response of the DiaCCon electrode after electrochemical activation. The sensitivity of the Imec electrode was insufficient within the investigated molarities to even provide an estimation.
For the DiaCCon electrode, after electrochemical activation, enough NVP peak behaviour was scavenged to make an estimation (as observed in Figure 5.24), using the reference signals obtained, standard deviations were calculated for each electrode during the normal and electrochemically activated procedure. These are listed in Table 5.4.

Table 5.4: Standard deviations obtained for the different DPV procedures.[a]

Electrode sample	σ of the normal reference in $\delta\mu A$	σ of the activated reference in $\delta\mu A$
DiaCCon	0.0038	0.2119
Imec	0.1822	15.1647

[a] the normal reference sample size is 6 DPV procedures while the activated reference only has 4. Under ordinary circumstances 10 reference measurements are suggested as minimum.

The identifiable peaks at the first scan on the DiaCCon electrode for different molarities (illustrated in Figure 5.23) were used to fit a linear regression and estimate the LOD and LOQ, with the results listed in Table 5.5.

[1] Linear ranges obtained on electrodes in literature are listed in Table 2.1, and the variety observed suggest that further study and proper tuning of the electrochemical activation procedure and DPV procedure is necessary in order to establish a linear regime for sensing NVP on BDD.

Table 5.5: Estimates of the standard deviation and sensitivity limits obtained by comparing the reference standard deviation and a linear regression (x1, y0) of the peaks observed in Figure 5.23, indicative of the first DPV scan after electrochemical activation.

x1	y_0 (μM)	σ_{x1}	σ_{y_0} (μM)	r	σ_{Ref} $(\delta \mu A)$	LOD_{Est} (μM)	LOQ_{Est} (μM)
0.048	0.887	0.048	0.054	0.998	0.212	13.3	44.3

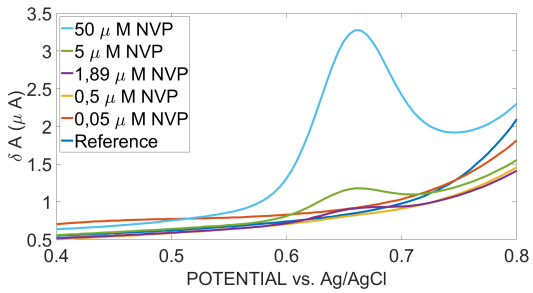

Figure 5.23: NVP peaks in different molarities on the DiaCCon electrode for the first scan after the first cathodic activation step

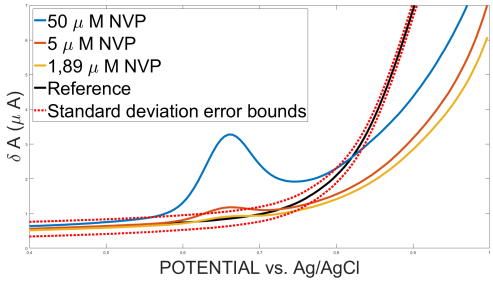

Figure 5.24: Standard error from table 5.4 visualized on the DiaCCon electrode in red over the black reference signal with NVP responses of different molarities in the first scan.

DPV detection in 0.1 M Na_2SO_4 with 5 and 10 μM NVP revealed peak recovery as in PBS (X1) (e.g. of electrochemical activation recovering peak behaviour in Figure 7.11 in Chapter 7). This confirms the general behaviour exhibited is not electrolyte dependent, and further suggests the inhibiting effect was not caused by electrolyte interactions, but is caused by NVP inhibiting the electrode surface or the electrode surface interaction with NVP. The quick lowering of the absorption profile at the DiaCCon electrode in 0.39 M Na_2SO_4 but subsequent non-activity suggests the activity is not the result of a classical degradation profile.

Chapter 6

Conclusions

After experimentation, several conclusions can be made in regard to the use of BDD electrodes for NVP sensing and degradation as well as the desirability of different surface properties. Characterisation of the BDD surfaces revealed a marked difference in $\frac{sp^3}{sp^2}$ ratio, while the surface topography difference was negligible. The electrochemical properties of the electrodes were investigated. The DiaCCon electrode (micro-crystalline DiaCCon BDD) revealed superior performance in both the attempted detection and degradation. The lower background current and higher $\frac{sp^3}{sp^2}$ ratio seem to have benefited the electrode considerably compared to the Imec electrode (nano-crystalline BDD) counterpart. The characterisation derived from the electrochemical redox couples and EIS appeared inconclusive, partly due to problems finding a correct combination of model and fit to properly describe the electrode surface.

The degradation of NVP was not achieved during this study. EAOP treatment of NVP proved to have effects contrary to expectations. The NVP compound resisted attempts to degrade in sodium sulfate, and showed minor changes in sodium chloride indicated by bathochromic shifts in the UV-Vis spectrum. The behaviour of NVP under the EAOP conditions used in this work implies the non-viability of EAOP using BDD to remove NVP from water. The responses induced by EAOP appear dependent on the electrolytes used. In a solution containing chloride, a bathochromic shift to a wavelength of around 307 nm was observed in the UV-Vis response of the characteristic peak originally at 282 nm. This change was more pronounced during degradation attempts with the micro-crystalline BDD electrode, but was also visible using the nano-crystalline BDD electrode.

The attempted degradation process was followed by a sensing study in PBS (X1). During experiments to accurately sense NVP on BDD electrodes, an inhibiting effect of NVP on electrochemical responses was observed. Repeated scans lowered the detected NVP peak, showing non-repeatable and non-reversible behaviour. Detection on the DiaCCon electrode and Imec electrode only proved possible at high molarities of NVP (e.g 50 μM), with the DiaCCon electrode having a preferable response with more pronounced peak behaviour. DPV optimization was attempted but rendered unfeasible due to the inhibiting effect of NVP on the peak response behaviour.

An in-situ electrochemical activation procedure (-2 V for 10 s) was thus deployed to combat the observed loss of sensitivity and electrode inhibition. Electrochemical activation proved capable of regenerating surface functionality, indicating that the inhibiting behaviour was most likely related to either surface termination or surface fouling. After applying electrochemical activation, the response behaviour of both electrodes was recovered in varying molarities of NVP. The micro-crystalline BDD electrode proved more sensitive to NVP than the nano-crystalline BDD electrode. After recovering peak response, the DiaCCon BDD exhibited enough peak behaviour to allow an estimation of the LOD and LOQ. The estimated LOD was 13.3 μM. The DiaCCon BDD also proved substantially more resistant to degradation by the electrochemical procedures. After experimentation, the Imec electrode showed physical degradation, observable through SEM imaging. This indicates a lower potential lifespan for the Imec nano-crystalline BDD during electrochemical processes. Overall, although NVP degradation was not confirmed nor observed, detection of NVP using BDD was achieved despite NVP's inhibitive interaction with the electrodes. The DiaCCon microcrystaline BDD showed remarkable improvements in sensitivity and performed better in the degradation attempts by demonstrating electrochemical activity while presumably being limited by the same inhibiting effect of NVP as observed in detection and degradation attempts on the Imec electrode.

Chapter 7

Recommendations for future research

EAOP degradation using BDD electrodes in the diamond group of the PME department was investigated. Experimentation into both degradation and sensing of a topical micropollutant was initiated, but further research is needed to asses the effects of the chosen micropollutant.

- The inhibiting behaviour of NVP on a BDD electrode is potentially representative of either fouling effects as reported in literature by Teradal et al. [36] on a GCE or a preferential surface termination for the detection of NVP. This requires confirmation by studies focused on these respective effects. To confirm fouling, measurement techniques which can quantify fouling such as X-ray photoelectron spectroscopy (XPS) [66], silver deposition imaging [67] and potentially EIS [68, 69] could be deployed on a BDD electrode used in NVP solutions. The effects of BDD surface termination on NVP detection should be investigated by forcibly oxygen or hydrogen terminating clean BDD electrodes and using them to detect NVP. If the inhibiting effect occurs at both hydrogen and oxygen terminated BDD, specific anti-fouling terminations or functional groups could also be considered as a potential solution to this inhibiting behaviour.

- By either applying proper yet time-consuming cleaning procedures or optimizing the use of in-situ electrochemical activation, considerable gains could be made on the electrochemical detection of NVP on BDD. Estimates in this study show the detection potential of microcrystalline BDD even under suboptimal conditions. Electrochemical activation through pulse trains and other variations [13, 67] should also be considered as potential techniques to regenerate NVP detection and to extend the effective use of the BDD electrode. Intra- and inter-day precision, linearity and repeatability measurements are needed to be comparable to establish NVP detection literature.

- The potential degradation of NVP was not ruled out during this study, a more diverse array of electrolytes or combinations of AOP techniques could potentially be used to properly asses the removal of NVP from an aquatic environment. This would require further study into EAOP procedures that inhibit fouling behaviour or alternatively combined AOP techniques (Electro-Fenton processes, etc).

- Development of a good electrochemical flow cell with in-situ measurement could allow accessible repeated degradation attempts while allowing continuous measurements of micropollutant levels present.

- The influence of crystallinity, porosity and surface termination effects as well as NDC on EIS responses appear to be interesting for potential studies into the EIS response of different BDD surface compositions. Comparative studies could be performed using home-grown BDD electrodes that can be grown to specifications. The derivation and development of EIS fitting models that can accurately explain observed EIS responses on BDD is as of yet an ongoing field in need of further research.

- As of writing (pandemic), there exists a huge public interest in antivirals. Eventually, this overrepresentation will wane from the public eye, but antiviral compounds are perpetually necessary. Antiviral treatments are relevant for extended periods of time, and remain ubiquitous. Antivirals have only recently been diagnosed as micro-pollutants that potentially evade wastewater treatment, and NVP is but one of many antiviral substances. Research into the removal of antiviral substances from

the aquatic environment therefore carries public relevancy and remains a viable micro-pollutant choice for future studies despite the resistance exhibited by NVP in this work.

Acknowledgments

It has to be the height of irony that research into removing an antiviral compound gets complicated by a viral pandemic.

Nonetheless I would like to acknowledge Dr. J.G. Buijnsters, André Sartori and Zhichao Liu for their guidance and kind assistance. I would also like to extend thanks to Diwakar Suresh Babu for providing contact angle measurements and to the technical support staff at the precision mechanical engineering department at the Faculty of Mechanical, Maritime and Materials Engineering of TU Delft for their aid during the experiments. A special thanks also goes towards Y. Doekhi-Bennani of the sanitary engineering research group in the water management department at the faculty of Civil Engineering and Geosciences of TU Delft and their support staff as well as Agnieszka Kooijman and Maxine Ankora of the Corrosion Technology and Electrochemistry research group of the material science engineering department at TU Delft for providing access to specialized measuring equipment.

Bibliography

[1] C. Stamm, K. Räsänen, F.J. Burdon, F. Altermatt, J. Jokela, A. Joss, M. Ackermann, and R.I.L. Eggen. Chapter four - unravelling the impacts of micropollutants in aquatic ecosystems: Interdisciplinary studies at the interface of large-scale ecology. In Alex J. Dumbrell, Rebecca L. Kordas, and Guy Woodward, editors, *Large-Scale Ecology: Model Systems to Global Perspectives*, volume 55 of *Advances in Ecological Research*, pages 183 – 223. Academic Press, 2016. doi: https://doi.org/10.1016/bs.aecr.2016.07.002.

[2] Sreejon Das, Nillohit Mitra Ray, Jing Wan, Adnan Khan, Tulip Chakraborty, and Madhumita B. Ray. Micropollutants in wastewater: Fate and removal processes. In Robina Farooq and Zaki Ahmad, editors, *Physico-Chemical Wastewater Treatment and Resource Recovery*. IntechOpen. doi: 10.5772/65644.

[3] Jimoh O. Tijani, Ojo O. Fatoba, Godfrey Madzivire, and Leslie F. Petrik. A review of combined advanced oxidation technologies for the removal of organic pollutants from water. *Water, Air, & Soil Pollution*, 225(9):2102. ISSN 1573-2932. doi: 10.1007/s11270-014-2102-y.

[4] Yang Deng and Renzun Zhao. Advanced oxidation processes (AOPs) in wastewater treatment. *Current Pollution Reports*, 1(3):167–176. ISSN 2198-6592. doi: 10.1007/s40726-015-0015-z.

[5] Christos Comninellis and Guohua Chen. *Electrochemistry for the environment*. Springer-Verlag, 1 edition. doi: 10.1007/978-0-387-68318-8.

[6] Robert B. More, Axel D. Haubold, and Jack C. Bokros. Chapter i.2.8 - pyrolytic carbon for long-term medical implants. In Buddy D. Ratner, Allan S. Hoffman, Frederick J. Schoen, and Jack E. Lemons, editors, *Biomaterials Science (Third Edition)*, pages 209–222. Academic Press. ISBN 978-0-12-374626-9. doi: 10.1016/B978-0-08-087780-8.00023-1.

[7] Julie V. Macpherson. A practical guide to using boron doped diamond in electrochemical research. *Physical Chemistry Chemical Physics*, 17(5):2935–2949. ISSN 1463-9084. doi: 10.1039/C4CP04022H. Publisher: The Royal Society of Chemistry.

[8] Sondos Dbira, Nasr Bensalah, Mohammad I. Ahmad, and Ahmed Bedoui. Electrochemical oxidation/-disinfection of urine wastewaters with different anode materials. *Materials*, 12(8), 2019. ISSN 1996-1944. doi: 10.3390/ma12081254.

[9] J.-P. Lagrange, A. Deneuville, and E. Gheeraert. Activation energy in low compensated homoepitaxial boron-doped diamond films1paper presented at the diamond 1997 conference.1. *Diamond and Related Materials*, 7(9):1390 – 1393, 1998. ISSN 0925-9635. doi: https://doi.org/10.1016/S0925-9635(98)00225-8.

[10] Oleksandra Ganzenko, David Huguenot, Eric D. van Hullebusch, Giovanni Esposito, and Mehmet A. Oturan. Electrochemical advanced oxidation and biological processes for wastewater treatment: a review of the combined approaches. *Environmental Science and Pollution Research*, 21(14):8493–8524. ISSN 1614-7499. doi: 10.1007/s11356-014-2770-6.

[11] S.A. Alves, T.C.R. Ferreira, N.S. Sabatini, A.C.A. Trientini, F.L. Migliorini, M.R. Baldan, N.G. Ferreira, and M.R.V. Lanza. A comparative study of the electrochemical oxidation of the herbicide tebuthiuron using boron-doped diamond electrodes. *Chemosphere*, 88(2):155 – 160, 2012. ISSN 0045-6535. doi: https://doi.org/10.1016/j.chemosphere.2012.02.042.

[12] Sean T. McBeath, David P. Wilkinson, and Nigel J. D. Graham. Application of boron-doped diamond electrodes for the anodic oxidation of pesticide micropollutants in a water treatment process: a critical review. *Environ. Sci.: Water Res. Technol.*, 5:2090–2107, 2019. doi: 10.1039/C9EW00589G.

[13] Benjamin L. Hanssen, Shajahan Siraj, and Danny K.Y. Wong. Recent strategies to minimise fouling in electrochemical detection systems. *Reviews in Analytical Chemistry*, 35(1):1 – 28, 2016. doi: https://doi.org/10.1515/revac-2015-0008.

[14] Raphaël Trouillon, Danny O'Hare, and Yasuaki Einaga. Effect of the doping level on the biological stability of hydrogenated boron doped diamond electrodes. *Phys. Chem. Chem. Phys.*, 13:5422–5429, 2011. doi: 10.1039/C0CP02420A.

[15] Inga Shpilevaya and John S. Foord. Electrochemistry of methyl viologen and anthraquinonedisulfonate at diamond and diamond powder electrodes: The influence of surface chemistry. *Electroanalysis*, 26(10): 2088–2099, 2014. doi: 10.1002/elan.201400310.

[16] Danyelle Medeiros de Araújo, Pablo Cañizares, Carlos A. Martínez-Huitle, and Manuel Andrés Rodrigo. Electrochemical conversion/combustion of a model organic pollutant on bdd anode: Role of sp3/sp2 ratio. *Electrochemistry Communications*, 47:37 – 40, 2014. ISSN 1388-2481. doi: https://doi.org/10.1016/j.elecom.2014.07.017.

[17] L. Carolina Espinoza, Adolfo Henríquez, David Contreras, and Ricardo Salazar. Evidence for the production of hydroxyl radicals at boron-doped diamond electrodes with different sp3/sp2 ratios and its relationship with the anodic oxidation of aniline. *Electrochemistry Communications*, 90:30 – 33, 2018. ISSN 1388-2481. doi: https://doi.org/10.1016/j.elecom.2018.03.007.

[18] Takeshi Watanabe, Satoru Yoshioka, Tomokazu Yamamoto, Hossein Sepehri-Amin, Tadakatsu Ohkubo, Syo Matsumura, and Yasuaki Einaga. The local structure in heavily boron-doped diamond and the effect this has on its electrochemical properties. *Carbon*, 137:333 – 342, 2018. ISSN 0008-6223. doi: https://doi.org/10.1016/j.carbon.2018.05.026.

[19] Sergi Garcia-Segura, Elisama Vieira dos Santos, and Carlos Alberto Martínez-Huitle. Role of sp3/sp2 ratio on the electrocatalytic properties of boron-doped diamond electrodes: A mini review. *Electrochemistry Communications*, 59:52 – 55. ISSN 1388-2481. doi: https://doi.org/10.1016/j.elecom.2015.07.002.

[20] Nagappa L. Teradal and J. Seetharamappa. Bulk modification of carbon paste electrode with bi2o3 nanoparticles and its application as an electrochemical sensor for selective sensing of antiHIV drug nevirapine. *Electroanalysis*, 27(8):2007–2016. ISSN 1521-4109. doi: 10.1002/elan.201500088.

[21] Anna Maria Cammett, Thomas R. MacGregor, Jan M. Wruck, Franco Felizarta, Patrick Miailhes, Josep Mallolas, and Peter J. Piliero. Pharmacokinetic assessment of nevirapine and metabolites in human immunodeficiency virus type 1-infected patients with hepatic fibrosis. *Antimicrobial Agents and Chemotherapy*, 53(10):4147–4152. ISSN 0066-4804. doi: 10.1128/AAC.00460-09.

[22] P. Riska, M. Lamson, T. MacGregor, J. Sabo, S. Hattox, J. Pav, and J. Keirns. Disposition and biotransformation of the antiretroviral drug nevirapine in humans. *Drug Metabolism and Disposition: The Biological Fate of Chemicals*, 27(8):895–901. ISSN 0090-9556.

[23] Timothy Paul Wood, Cornelia S. J. Duvenage, and Egmont Rohwer. The occurrence of anti-retroviral compounds used for HIV treatment in south african surface water. *Environmental Pollution*, 199: 235–243, . ISSN 0269-7491. doi: 10.1016/j.envpol.2015.01.030.

[24] Elijah Ngumba, Anthony Gachanja, and Tuula Tuhkanen. Occurrence of selected antibiotics and antiretroviral drugs in nairobi river basin, kenya. *Science of The Total Environment*, 539:206–213. ISSN 0048-9697. doi: 10.1016/j.scitotenv.2015.08.139.

[25] Carsten Prasse, Michael P. Schlüsener, Ralf Schulz, and Thomas A. Ternes. Antiviral drugs in wastewater and surface waters: a new pharmaceutical class of environmental relevance? *Environmental Science & Technology*, 44(5):1728–1735. ISSN 0013-936X. doi: 10.1021/es903216p.

[26] Swati Jain, Pardeep Kumar, Raj K. Vyas, Prabhat Pandit, and Ajay K. Dalai. Occurrence and removal of antiviral drugs in environment: A review. *Water, Air, & Soil Pollution*, 224(2):1410. ISSN 1573-2932. doi: 10.1007/s11270-012-1410-3.

[27] Somandla Ncube, Lawrence M. Madikizela, Luke Chimuka, and Mathew M. Nindi. Environmental fate and ecotoxicological effects of antiretrovirals: A current global status and future perspectives. *Water Research*, 145:231–247. ISSN 0043-1354. doi: 10.1016/j.watres.2018.08.017.

[28] Marie Clémentine U. Nibamureke, Irene E. J. Barnhoorn, and Gesina M. Wagenaar. Assessing the potential effects of nevirapine in south african surface water on fish growth: A chronic exposure of oreochromis mossambicus. *South African Journal of Science*, 115(3):1–6. ISSN 0038-2353. doi: 10.17159/sajs.2019/5516. Publisher: Academy of Science of South Africa.

[29] Timothy Paul Wood, Adriaan Erasmus Basson, Cornelia Duvenage, and Egmont Richard Rohwer. The chlorination behaviour and environmental fate of the antiretroviral drug nevirapine in south african surface water. *Water Research*, 104:349–360, . ISSN 1879-2448. doi: 10.1016/j.watres.2016.08.038.

[30] Fenfen Zhang, Li Li, Liqiang Luo, Yaping Ding, and Xiao Liu. Electrochemical oxidation and determination of antiretroviral drug nevirapine based on uracil-modified carbon paste electrode. *Journal of Applied Electrochemistry*, 43(3):263–269. ISSN 1572-8838. doi: 10.1007/s10800-012-0516-z.

[31] Arnaldo Aguiar Castro, Ricardo Queiroz Aucelio, Nicolas Adrian Rey, Eliane Monsores Miguel, and Percio Augusto Mardini Farias. Determination of the antiretroviral drug nevirapine in diluted alkaline electrolyte by adsorptive stripping voltammetry at the mercury film electrode. *Combinatorial Chemistry & High Throughput Screening*, 14(1):22–27.

[32] Elahe Ahmadi, Mohamad Reza Eyvani, Vahid Riahifar, Hossein Momeneh, and Changiz Karami. Amperometric determination of nevirapine by GCE modified with c-MWCNTs and synthesized 11-mercaptoundecanoyl hydrazinecarbothioamide coated silver nanoparticles. *Microchemical Journal*, 146: 1218–1226. ISSN 0026-265X. doi: 10.1016/j.microc.2019.02.054.

[33] Daniel Apath, Mambo Moyo, and Munyaradzi Shumba. TiO2 nanoparticles decorated graphene nanoribbons for voltammetric determination of an anti-HIV drug nevirapine. *Journal of Chemistry*. ISSN 2090-9063. doi: https://doi.org/10.1155/2020/3932715.

[34] Mohammad Bagher Gholivand, Elahe Ahmadi, and Mozhdeh Haseli. A novel voltammetric sensor for nevirapine, based on modified graphite electrode by MWCNs/poly(methylene blue)/gold nanoparticle. *Analytical Biochemistry*, 527:4–12. ISSN 0003-2697. doi: 10.1016/j.ab.2017.03.018.

[35] Saeed Shahrokhian, Razieh Kohansal, Masoumeh Ghalkhani, and Mohammad K. Amini. Electrodeposition of copper oxide nanoparticles on precasted carbon nanoparticles film for electrochemical investigation of anti-HIV drug nevirapine. *Electroanalysis*, 27(8):1989–1997. ISSN 1521-4109. doi: 10.1002/elan.201500027.

[36] Nagappa Laxman Teradal, Shankar Narayan Prashanth, and Jaldappagari Seetharamappa. Electrochemical studies of nevirapine, an anti-HIV drug, and its assay in tablets and biological samples. *Journal of Electrochemical Science and Engineering*, 2(2):67–75. doi: 10.5599/jese.2012.0008.

[37] Ana Esteva, Elias Blanco, Juan Pina, Abel Balbin, Carmen Quintana, and Pedro Hernandez. Determination of nevirapine in the presence of cucurbit(7)uril with a gold electrode. *Journal of Electrochemical Science and Engineering*, 4(1):37–44. doi: 10.5599/jese.2014.0043.

[38] Ali S. Ali. Application of nanomaterials in environmental improvement. doi: 10.5772/intechopen.91438. url: https://www.intechopen.com/online-first/application-of-nanomaterials-in-environmental-improvement
Accessed on 2020-07-12.

[39] Jorge A. Montes-Gutiérrez, Jesús J. Alcantar-Peña, Elida de Obaldia, Nancy J. Zúñiga-Rivera, Valery Chernov, Rodrigo Meléndrez-Amavizca, Marcelino Barboza-Flores, Rafael Garcia-Gutierrez, and Orlando Auciello. Afterglow, thermoluminescence and optically stimulated luminescence characterization of micro-, nano- and ultrananocrystalline diamond films grown on silicon by HFCVD. *Diamond and Related Materials*, 85:117–124. ISSN 0925-9635. doi: 10.1016/j.diamond.2018.03.031.

[40] Atomic force microscopy working principle — AFM explained - nanosurf. https://www.nanosurf.com/en/support/afm-operating-principle. Accessed: 2020-07-12.

[41] André F. Sartori, Stefano Orlando, Alessandro Bellucci, Daniele M. Trucchi, Shoshan Abrahami, Thijs Boehme, Thomas Hantschel, Wilfried Vandervorst, and Josephus G. Buijnsters. Laser-induced periodic surface structures (lipss) on heavily boron-doped diamond for electrode applications. *ACS Applied Materials & Interfaces*, 10(49):43236–43251, 2018. doi: 10.1021/acsami.8b15951.

[42] Koichi Ushizawa, Kenji Watanabe, Toshihiro Ando, Isao Sakaguchi, Mikka Nishitani-Gamo, Yoichiro Sato, and Hisao Kanda. Boron concentration dependence of raman spectra on 100 and 111 facets of b-doped cvd diamond. *Diamond and Related Materials*, 7(11):1719 – 1722, 1998. ISSN 0925-9635. doi: https://doi.org/10.1016/S0925-9635(98)00296-9.

[43] Petros Xanthopoulos, Georgios Pyrgiotakis, Stephen Grobmyer, P. Pardalos, and Larry Hench. Raman spectroscopy for clinical oncology. *Advances in Optical Technologies*, 2011:1–20, 2011. doi: 10.1155/2011/213783.

[44] Ossila Ltd. Cyclic voltammetry: Basics explained. url: https://www.ossila.com/pages/cyclic-voltammetry
Acessed on 2020-07-12.

[45] Edward P. Randviir. A cross examination of electron transfer rate constants for carbon screen-printed electrodes using electrochemical impedance spectroscopy and cyclic voltammetry. *Electrochimica Acta*, 286:179–186. ISSN 0013-4686. doi: 10.1016/j.electacta.2018.08.021.

[46] R. S. Nicholson. Theory and application of cyclic voltammetry for measurement of electrode reaction kinetics. *Analytical Chemistry*, 37(11):1351–1355. ISSN 0003-2700. doi: 10.1021/ac60230a016. Publisher: American Chemical Society.

[47] Zoski Cynthia G. *Handbook of Electrochemistry*. Elsevier. ISBN 978-0-444-51958-0. doi: 10.1016/B978-0-444-51958-0.X5000-9.

[48] Renato Seeber, Chiara Zanardi, and György Inzelt. Links between electrochemical thermodynamics and kinetics. *ChemTexts*, 1(4):18. ISSN 2199-3793. doi: 10.1007/s40828-015-0018-9.

[49] D. A. Dornbusch, R. Hilton, M. J. Gordon, and G. J. Suppes. Effects of sonication on EIS results for zinc alkaline batteries. *ECS Electrochemistry Letters*, 2(9):A89–A92, jun 2013. doi: 10.1149/2.006309eel.

[50] Gaurab Dutta, Shabnam Siddiqui, Hongjun Zeng, John A. Carlisle, and Prabhu U. Arumugam. The effect of electrode size and surface heterogeneity on electrochemical properties of ultrananocrystalline diamond microelectrode. *Journal of Electroanalytical Chemistry*, 756:61 – 68, 2015. ISSN 1572-6657. doi: https://doi.org/10.1016/j.jelechem.2015.08.016.

[51] Brian P. Chaplin, Ian Wyle, Hongjun Zeng, John A. Carlisle, and James Farrell. Characterization of the performance and failure mechanisms of boron-doped ultrananocrystalline diamond electrodes. *Journal of Applied Electrochemistry*, 41(11):1329. ISSN 1572-8838. doi: 10.1007/s10800-011-0351-7.

[52] Shimadzu Scientific Instruments. Uv-vis frequently asked questions - instrument design. url: `https://www.ssi.shimadzu.com/`. Accessed on 2020-08-14.

[53] Laurence M. Harwood and Thimothy D.W. Claridge. *Introduction to Organic Spectroscopy*. Oxford University Press Inc., New York, New York, 1997. ISBN 978-0-19-8557755-5. 2011 reprinted edition.

[54] Pratik Ranaware, A.M. Ingle, A. Ladke, A.R. Madgulkar, and Mrinalini Damle. Determination of nevirapine in human plasma by hplc. *Journal of Chemical and Pharmaceutical Research*, 4:3003–3009, 01 2012.

[55] Fritz Scholz. Voltammetric techniques of analysis: the essentials. *ChemTexts*, 1(4):17. ISSN 2199-3793. doi: 10.1007/s40828-015-0016-y.

[56] F. R. Simões and M. G. Xavier. 6 - electrochemical sensors. In Alessandra L. Da Róz, Marystela Ferreira, Fábio de Lima Leite, and Osvaldo N. Oliveira, editors, *Nanoscience and its Applications*, Micro and Nano Technologies, pages 155–178. William Andrew Publishing. ISBN 978-0-323-49780-0. doi: 10.1016/B978-0-323-49780-0.00006-5.

[57] V. Mortet, A. Taylor, Z. Vlčková Živcová, D. Machon, O. Frank, P. Hubík, D. Tremouilles, and L. Kavan. Analysis of heavily boron-doped diamond raman spectrum. *Diamond and Related Materials*, 88:163 – 166, 2018. ISSN 0925-9635. doi: https://doi.org/10.1016/j.diamond.2018.07.013.

[58] Michael C. Granger, Malgorzata Witek, Jishou Xu, Jian Wang, Mateusz Hupert, Amy Hanks, Miles D. Koppang, James E. Butler, Guy Lucazeau, Michel Mermoux, Jerzy W. Strojek, and Greg M. Swain. Standard electrochemical behavior of high-quality, boron-doped polycrystalline diamond thin-film electrodes. *Analytical Chemistry*, 72(16):3793–3804, 2000. doi: 10.1021/ac0000675. PMID: 10959965.

[59] Michael C. Granger and Greg M. Swain. The influence of surface interactions on the reversibility of ferri/ferrocyanide at boron-doped diamond thin-film electrodes. *Journal of The Electrochemical Society*, 146(12):4551. ISSN 1945-7111. doi: 10.1149/1.1392673. Publisher: IOP Publishing.

[60] Ch. Dharmaraju, P. Hiranmayi, K.V. Himavani, K. Prabhavathi, Mishra Rosaline, and J.S. Srinivas. Spectrophotometric determination of nevirapine in bulk drugsand its forced degradation studies. *Journal of Pharmacy Research 2*, 4:2910–2912, 2011. ISSN 0974-6943.

[61] Jing Ding, Lingjun Bu, Qingliang Zhao, Felix Tetteh Kabutey, Liangliang Wei, and Dionysios D. Dionysiou. Electrochemical activation of persulfate on bdd and dsa anodes: Electrolyte influence, kinetics and mechanisms in the degradation of bisphenol a. *Journal of Hazardous Materials*, 388:121789, 2020. ISSN 0304-3894. doi: https://doi.org/10.1016/j.jhazmat.2019.121789.

[62] Ervin Nurhayati. A brief review on electro-generated hydroxyl radical for organic wastewater mineralization. *Jurnal Sains Teknologi Lingkungan*, 4:24–31, 03 2012. doi: 10.20885/jstl.vol4.iss1.art3.

[63] R. Kiran, Emmanuel Scorsone, Jacques Sanoit (de), Jean-Charles Arnault, P. Mailley, and P. Bergonzo. Boron Doped Diamond Electrodes for Direct Measurement in Biological Fluids: An In Situ Regeneration Approach. *Journal of The Electrochemical Society*, 160(1):H67 – H73, November 2012. doi: 10.1149/2.014302jes.

[64] Giancarlo R. Salazar-Banda, Adriana E. de Carvalho, Leonardo S. Andrade, Romeu C. Rocha-Filho, and Luis A. Avaca. On the activation and physical degradation of boron-doped diamond surfaces brought on by cathodic pretreatments. *Journal of Applied Electrochemistry*, 40(10):1817–1827. ISSN 1572-8838. doi: 10.1007/s10800-010-0139-1.

[65] Ricardo F. Brocenschi, Romeu C. Rocha-Filho, Boris Duran, and Greg M. Swain. The analysis of estrogenic compounds by flow injection analysis with amperometric detection using a boron-doped diamond electrode. *Talanta*, 126:12 – 19, 2014. ISSN 0039-9140. doi: https://doi.org/10.1016/j.talanta.2014.02.047.

[66] Pumidech Puthongkham, Scott T. Lee, and B. Jill Venton. Mechanism of histamine oxidation and electropolymerization at carbon electrodes. *Analytical chemistry*, 91(13):8366–8373. ISSN 0003-2700. doi: 10.1021/acs.analchem.9b01178.

[67] An-Yi Chang, Gaurab Dutta, Shabnam Siddiqui, and Prabhu U. Arumugam. Surface fouling of ultrananocrystalline diamond microelectrodes during dopamine detection: Improving lifetime via electrochemical cycling. *ACS Chemical Neuroscience*, 10(1):313–322, 2019. doi: 10.1021/acschemneuro.8b00257. PMID: 30285418.

[68] Xiao-Mei Wang, Ji-Ming Hu, Jian-Qing Zhang, and Chu-Nan Cao. Characterization of surface fouling of ti/iro2 electrodes in 4-chlorophenol aqueous solutions by electrochemical impedance spectroscopy. *Electrochimica Acta*, 53(8):3386 – 3394, 2008. ISSN 0013-4686. doi: https://doi.org/10.1016/j.electacta.2007.11.070.

[69] Ronnie Anseth, Nils-Olav Skeie, and Magne Waskaas. Preliminary studies on monitoring fouling layers on a charged electrode using electrical impedance spectroscopy. *tm - Technisches Messen*, 85, 01 2018. doi: 10.1515/teme-2017-0129.

Appendices

Figures and tables

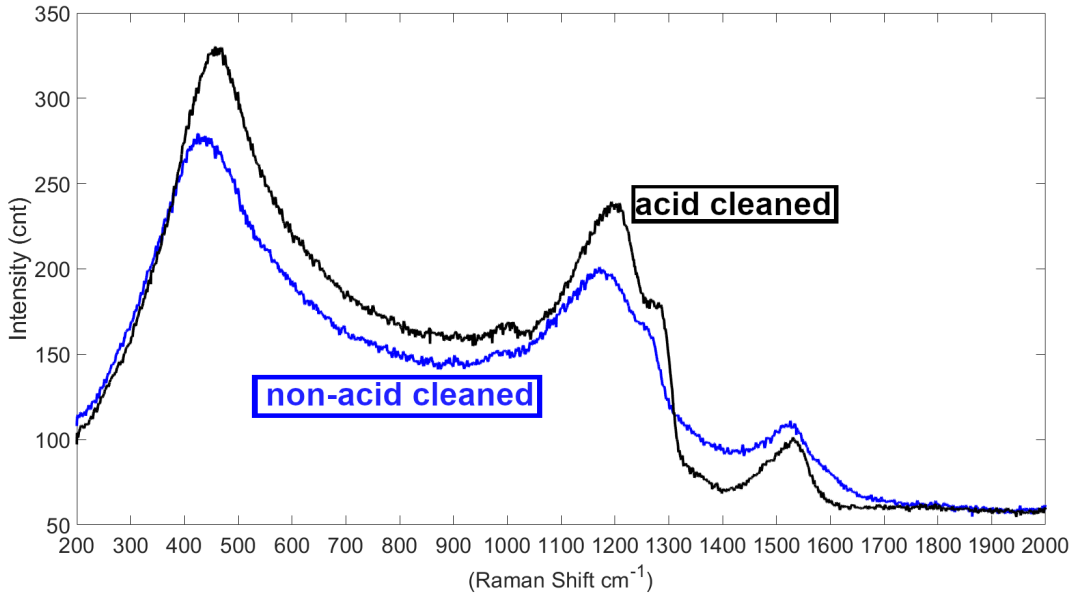

Figure 7.1: Raman spectrums obtained from representative Imec electrodes used in Section 4.4 to illustrate the effects of acid cleaning. Acquisition time was 5 seconds instead of the settings reported in Section 4.7. Measurements were made during the same run.

Table 7.1: EIS circuit fitting results for the DiaCCon electrode with 1mM ferrocyanide and 1mM ruhex in 0.1 M KNO_3

EIS circuit model results	Redox species	R_s (Ω)	Q_0 ($s^n/\Omega * 10^9$) (CPE_{dl})	n_q (CPE_{dl}	R_{CT} in (Ω)	R_{sp} ($k\Omega$)	$Q_0 s^n/\Omega * 10^6$ from (CPE_Q)	n_q from (CPE_Q)	$\chi^2 x10^4$
DiaCCon	ferrocyanide	20	461	0.95	83	0.975	3.7	0.99	4.7
	ruhex	19.9	0.337	1	84	46.578	143.4	0.99	200

Table 7.2: EIS circuit fitting results for the Imec electrode with 1mM ferrocyanide and 1mM ruhex in 0.1 M KNO_3

EIS circuit model results	Redox species	R_s (Ω)	Q_0 ($s^n/\Omega * 10^8$) (CPE_{dl})	n_q (CPE_{dl}	R_{CT} (Ω)	Q_0 in $s^n/\Omega * 10^6$ from (CPE_W)	n_q from (CPE_W	$\chi^2 x10^2$
Imec	ferrocyanide	20.9	2.5	1.2	41.8	1230	0.33	9.06
	ruhex	3570	75.3	0.2	-0.005	6.31	0.88	0.25

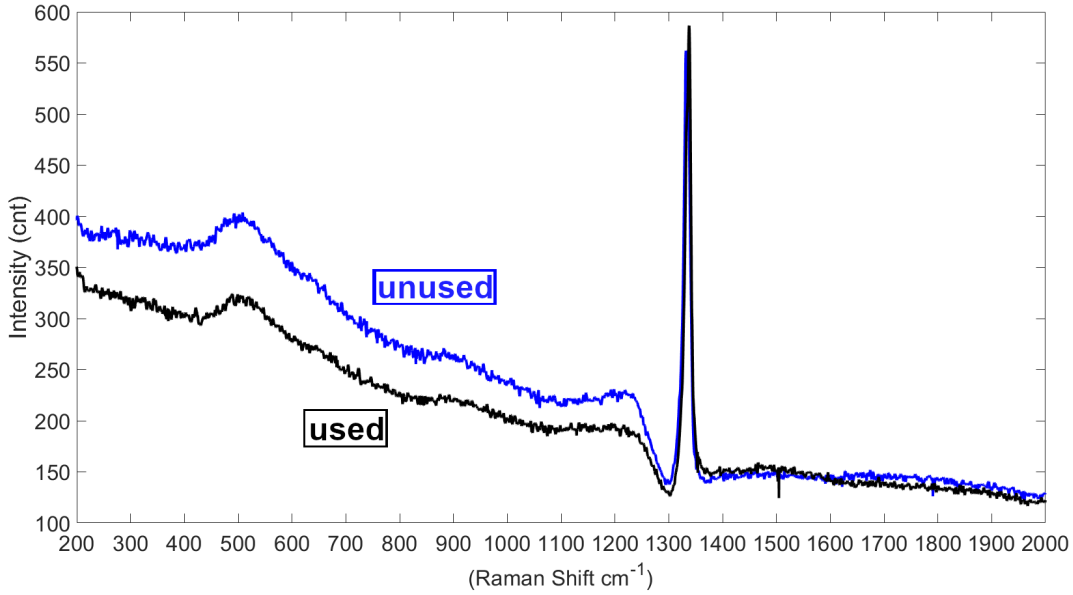

Figure 7.2: Raman spectrums obtained from the DiaCCon electrode after use and representative as-grown samples. Measurements were made during the same run.

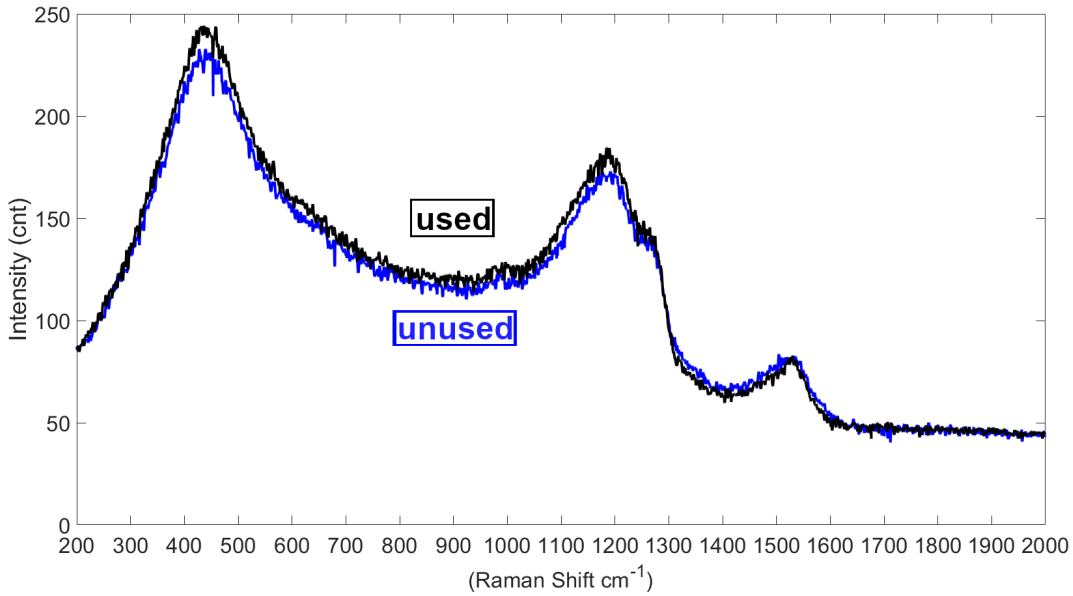

Figure 7.3: Raman spectrums obtained from the Imec electrode after use and representative as-grown samples. Measurements were made during the same run.

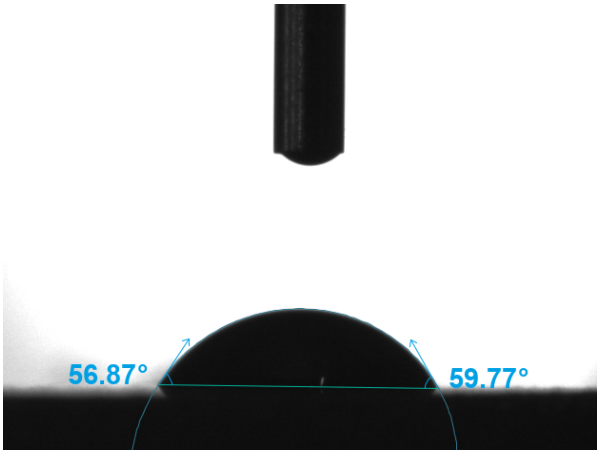

Figure 7.4: Contact angle measurement on the used DiaCCon electrode.

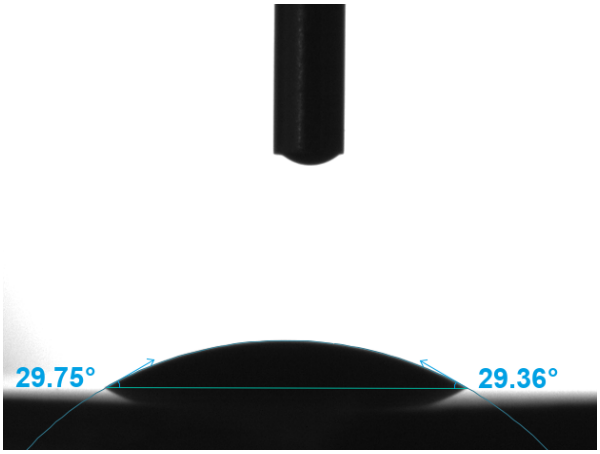

Figure 7.5: Contact angle measurement on the used Imec electrode.

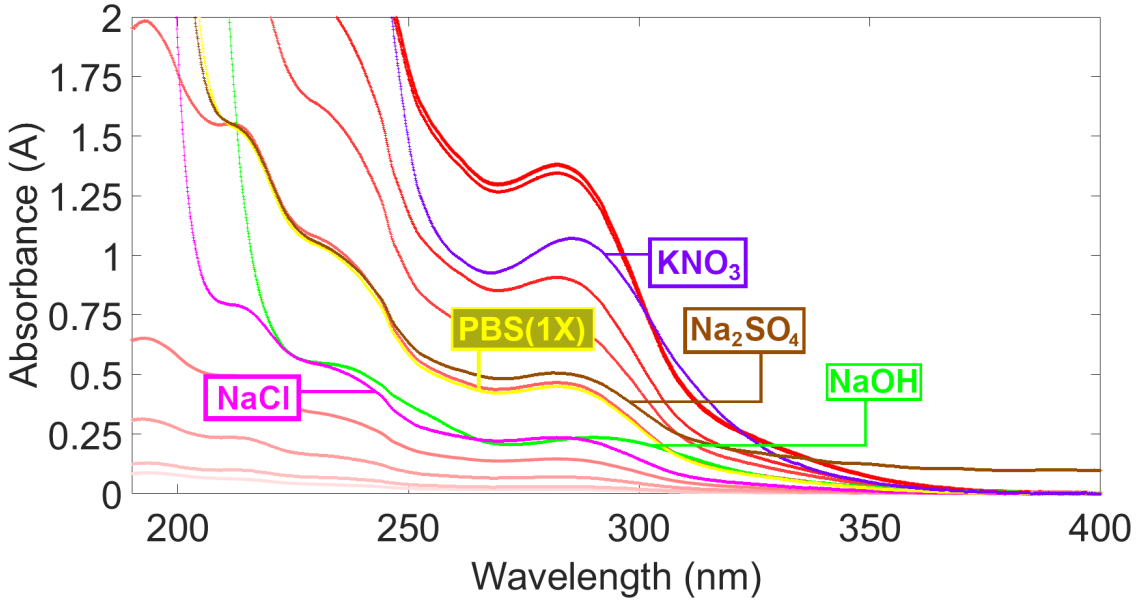

Figure 7.6: The effect of different electrolytes on a blank NVP response in UV-Vis spectroscopy.

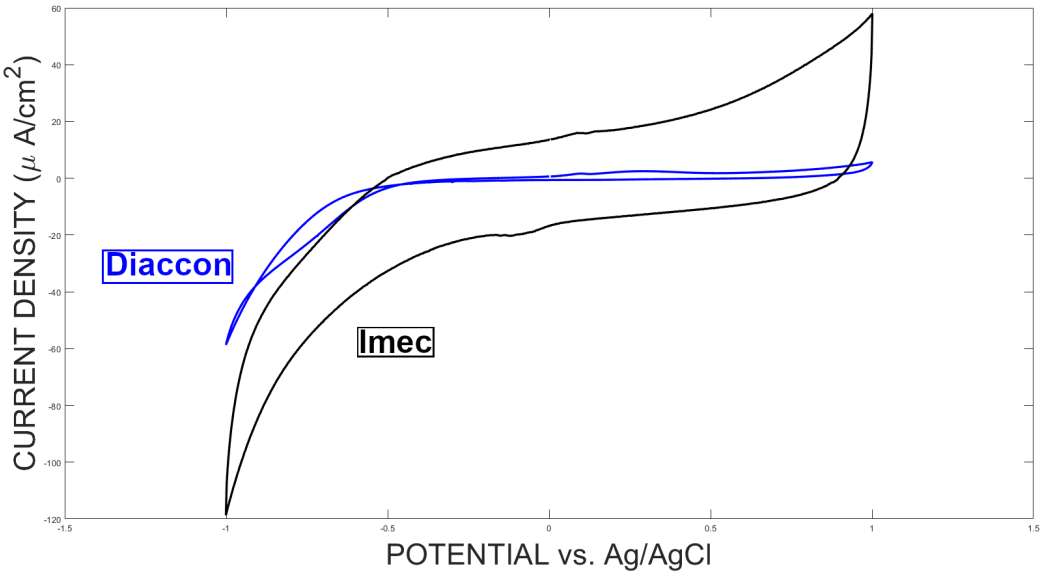

Figure 7.7: CV in PBS (X1) with a scan rate of 0.1 V/s for both the Imec and DiaCCon electrode. Scans taken at the 5th cycle.

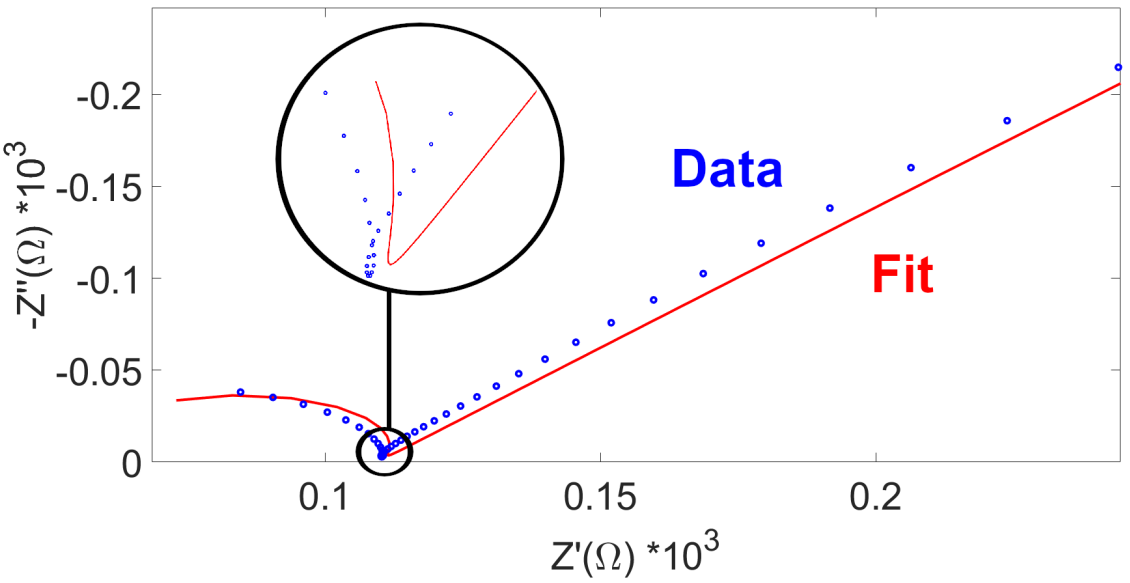

Figure 7.8: Zoomed version of the EIS results of the DiaCCon electrode in 1mM ruhex and 0.1 M KNO_3.

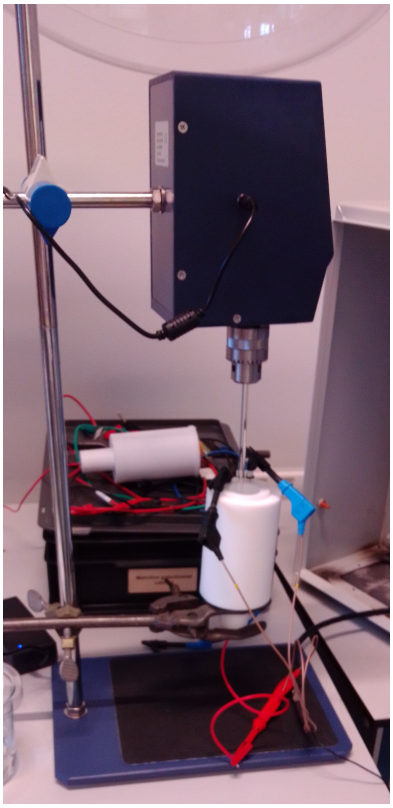

Figure 7.9: A photo of the setup used for degradation.

Figure 7.10: A photo of the setup used for detection with the Faraday cage open.

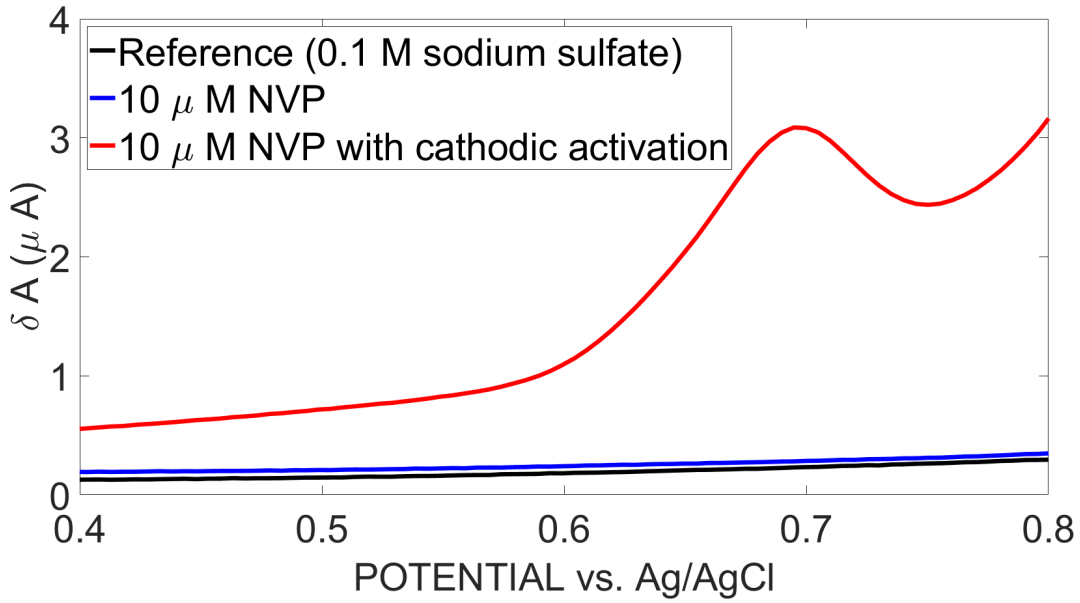

Figure 7.11: DPV results in 0.1 M Na_2SO_4 using 10 μM NVP and a reference measurement, showing similar recovery behaviour as in PBS (1X).